The initial stages of ZnO atomic layer deposition on atomically flat In_0.53Ga_0.47As substrates

Evgeniy Skopin, Laetitia Rapenne, Hervé Roussel, Jean-Luc Deschanvres, Elisabeth Blanquet, Gianluca Ciatto, Dillon Fong, Marie-Ingrid Richard, Hubert Renevier

The Initial Stages of ZnO Atomic Layer Deposition on Atomically Flat $In_{0.53}Ga_{0.47}As$ Substrates

E.V. Skopin,[†] L. Rapenne,[†] H. Roussel,[†] J.L. Deschanvres,[†] E. Blanquet,[‡] G. Ciatto,[¶] D.D. Fong,[§] M.-I. Richard,[‖] and H. Renevier[*,†]

[†]*Université Grenoble Alpes, CNRS, Grenoble INP,[a] LMGP, F-38000 Grenoble, France*

[‡]*Université Grenoble Alpes, CNRS, Grenoble INP,[b] SIMAP, F-38000 Grenoble, France*

[¶]*Synchrotron SOLEIL - Beamline SIRIUS, L'Orme des Merisiers, Saint-Aubin, F-91192, Gif sur Yvette, France*

[§]*Materials Science Division, Argonne National Laboratory, 9700 S. Cass Ave., Argonne, Illinois 60439, United States*

[‖]*Aix-Marseille Université, CNRS, Université de Toulon, IM2NP UMR 7334, F-13397 Marseille, France; ID01, European Synchrotron Radiation Facility, F-38043 Grenoble, France*

E-mail: hubert.renevier@grenoble-inp.fr

[a]Institute of Engineering Univ. Grenoble Alpes
[b]Institute of Engineering Univ. Grenoble Alpes

Abstract

InGaAs is one of the III-V active semiconductors used in modern high-electron-mobility transistors or high-speed electronics. ZnO is a good candidate material to be inserted as a tunneling insulator layer at the metal-semiconductor junction. A key consideration in many modern devices is the atomic structure of the hetero-interface, which often ultimately governs

the electronic or chemical process of interest. Here, a complementary suite of *in situ* synchrotron X-ray techniques (fluorescence, reflectivity and absorption) as well as modeling is used to investigate both structural and chemical evolution during the initial growth of ZnO by atomic layer deposition (ALD) on $In_{0.53}Ga_{0.47}As$ substrates. Prior to steady-state growth behavior, we discover a transient regime characterized by two stages. First, substrate-inhibited ZnO growth takes place on InGaAs terraces. This leads eventually to the formation of a 1-nm-thick, two-dimensional (2D) amorphous layer. Second, the growth behavior and its modeling suggest the occurrence of dense island formation, with an aspect ratio and surface roughness that depends sensitively on the growth condition. Finally, ZnO ALD on $In_{0.53}Ga_{0.47}As$ is characterized by 2D steady-state growth with a linear growth rate of 0.21 nm.cy^{-1}, as expected for layer-by-layer ZnO ALD.

1 Introduction

The revolution in microelectronics has been accompanied by miniaturization of the silicon field-effect transistor (FET). While the transistor density and switching speeds have increased exponentially,[1] continued improvements will require greater cooling due to the larger power density; any decrease in operating voltage would lead to lower switching speeds.[2–4] One potential solution is the insertion of III-V materials into the metal-oxide-semiconductor FET (MOSFET) channel,[5] as they have higher carrier mobilities than silicon. A well-known candidate material is $In_{1-x}Ga_xAs$ or InGaAs, which has a carrier mobility value almost ten times higher than Si.[6–9] The ternary InGaAs alloy is a direct band gap semiconductor, and, by varying its composition, the band gap can be changed[10,11] from 0.354 eV (InAs) to 1.424 eV (GaAs). Furthermore, as the InGaAs band gap energies correspond to wavelengths in the near-infrared (IR) spectrum, this material can be used to create IR receivers and emitters,[12–14] high-power diode lasers,[15] devices for high-current electronics, and microwave electronics based on InGaAs/InP heterostructures.[16,17] Use of InGaAs as the channel material, however, will necessitate growth of a suitable oxide that can be employed as the gate dielectric while minimizing issues due to Fermi level pinning[18] such as a large contact

resistance.

Growth by atomic layer deposition (ALD) allows one to carefully control material thickness and create ultra-thin layers due to a self-limiting chemical reaction.[19] Many different gate oxide layers have already been grown on InGaAs-channel MOSFETs[20] by ALD: Al_2O_3,[21–23] HfO_2,[23–27] ZrO_2,[9] HfAlO,[23] and $LaAlO_3$.[28] Atomic layer deposition of Al_2O_3 even induces self-cleaning and removal of natural and uncontrolled oxides on the InGaAs surface.[29] While Al_2O_3 is one of the best candidates for InGaAs surface passivation, another thin layer between it and InGaAs (i.e., an interfacial passivation layer or IPL) that can suppress dielectric oxide crystallization and decrease leakage current and interface state density is highly desirable. Others have found that ALD-grown IPLs of Gd_2O_3 and Sc_2O_3 can result in higher dielectric constants than Al_2O_3 alone,[30] and a 0.4-nm-thick IPL of La_2O_3 promotes smaller hysteresis and lower gate leakage.[31] A thin layer of Al_2O_3 was used as an IPL in a HfTiO/Al_2O_3/InGaAs gate stack to reduce the interface state density and avoid Fermi level pinning at the HfTiO/InGaAs interface.[32] Here we investigate the growth of ZnO IPLs[33,34] by ALD on InGaAs,[34] which has already been shown to reduce the formation of both Ga and As oxides and depin the Fermi level in InGaAs-based MOSFETs.[35,36] In the study of low resistivity metal-insulator-semiconductors,[18] it has also been demonstrated that ZnO can act as a good tunnel barrier on InGaAs. The authors calculated that the minimum specific contact resistance for the Al/ZnO/InGaAs system requires a ZnO insulator thickness of only 0.6 nm. Atomic layer deposition, a cyclical deposition process based on self-terminating chemical reactions, is an ideal synthesis technique for the growth of inorganic materials in the nanometer thickness range. During steady state growth, each reactant species saturates and adsorbs to the growing surface such that the thickness per cycle is often close to one monolayer. However, there can be considerable variability in the initial stages, when surface saturation depends on the steric hindrance of the reactant ligands and the areal density of reactive sites.[37] The existence of fewer reactive sites on the substrate decreases the amount of deposited material per cycle and leads to the formation of 3D islands. This substrate-inhibited growth behavior[38] is typically observed for deposition on highly dissimilar materials,[38–44] resulting in a transient regime prior to the onset of

steady state growth. Importantly, the material deposited during this stage can strongly impact many properties of the resulting film, including its morphology, surface roughness, crystal structure, and conformity with the substrate, as well as determines the lowest achievable thickness for a continuous film.

For the synthesis of ultra-thin ZnO IPLs or tunnel barriers on InGaAs by ALD, it is therefore imperative to understand the different processes that take place at the interface during the first few cycles of deposition. We employ an *in situ* synchrotron X-ray approach that provides detailed structural and chemical insight during ALD.[45–47] Here, we report a detailed study on the structural and chemical evolution of ZnO layers grown by ALD on $In_{0.53}Ga_{0.47}As$ single crystal substrates, utilizing a custom-built chamber that permits the use of a variety of *in situ* synchrotron X-ray techniques. This allows us to monitor the incipient growth of ZnO ultra-thin films on atomically flat $In_{0.53}Ga_{0.47}As$ and determine the film structure cycle-by-cycle until steady state growth behavior is reached.

2 Experimental Section

2.1 Substrate preparation

The $In_{0.53}Ga_{0.47}As$ (001) substrates were provided by G.I.E III-V Lab (Palaiseau, France). Molecular beam epitaxy (MBE) was used to grow 270-nm-thick layers of $In_{0.53}Ga_{0.47}As$ on (001) InP substrates, with a 10-nm thick InP buffer layer. An illustration of the sample cross section is shown in Figure 1. The $In_{0.53}Ga_{0.47}As$ substrates were agitated in 4M HCl solution for 5 min to remove the native oxide,[48] rinsed in deionized water for 30 s, and then dried with argon before immediate introduction into the ALD reactor. The samples were then annealed at 200°C for 30 min in the reactor under a constant flow of 100 sccm nitrogen to evaporate As from the surface.

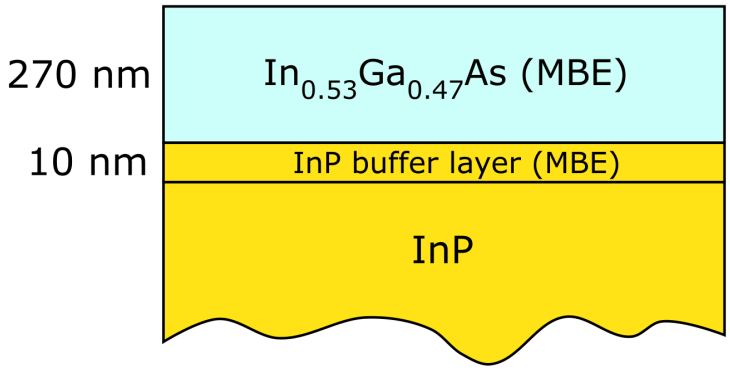

Figure 1: Schematic of the substrate cross section: ultra-thin ZnO layers are deposited on a 270-nm-thick $In_{0.53}Ga_{0.47}As$ film grown by MBE onto a 300-μm-thick InP (001) substrate with a 10-nm-thick InP buffer layer.

2.2 ALD reactor and parameters of deposition

Ultra-thin layers of ZnO were grown by ALD in a reactor specially designed for *in situ* X-ray studies.[49] Diethylzinc $Zn(C_2H_5)_2$ or DEZn was used as the Zn precursor (with the liquid maintained at 40°C) and room temperature H_2O employed as the oxidant; Argon and Nitrogen were used to purge the reactor and gas lines. We investigated three different substrate temperatures: 100°C, 120°C, and 140°C in the ALD window[50]. Each ALD cycle was comprised of the following steps: 1) DEZn vapor enters the chamber and reacts with the sample surface; 2) the chamber is purged with N_2, removing any residual precursor and reaction products; 3) H_2O vapor is introduced into the chamber, reacting with the surface; 4) the chamber is again purged with N_2 to remove any residual oxidant and reaction products. Prior to every introduction of precursor or oxidant, the pressure of the chamber was reduced, and the valve separating the chamber from the pump was closed. The flow of pure DEZn was 5 sccm for 5 s. The oxidant was either moist air or deionized water. The flow of moist air (resp. water) was 100 sccm for 10 s (3 sccm for 40 s). For the purging step, we maintained a N_2 flow of 1000 sccm for 45 s while the chamber was continually pumped.

2.3 *In situ* synchrotron X-ray measurements

The custom-built ALD reactor[49] is equipped with a polyether ether ketone (PEEK) window for *in situ* synchrotron X-ray measurements and counter-rotating flange to allow rotation of the sample but not the reactor body. The reactor was mounted onto a six-axis tower of a heavy-duty diffractometer (Newport) installed at the SIRIUS beamline of the SOLEIL synchrotron.[51] The beamline features a HU36 apple 2 undulator source, a Si(111) monochromator, and Pt-coated mirrors for harmonic rejection, providing a photon flux on the sample of $\sim 3 \times 10^{12}$ ph/s at 10 keV. X-ray reflectivity (XRR) and X-ray fluorescence (XRF) data were recorded at 10 keV (above the Zn K-edge at 9.659 keV) either during each ALD cycle or after the completion of several ALD cycles (without X-rays) while purging the reactor with a nitrogen flow of 100 sccm. The X-ray absorption spectroscopy measurements were performed across the Zn K-edge in fluorescence mode, using a four-element silicon drift detector (SDD) mounted 30° above the surface plane. The incidence angle was set to 1.7°, well above the critical angle for $In_{0.53}Ga_{0.47}As$ at 10 keV (0.25°). As the sample surface was nearly horizontal and the X-ray polarization was linear and horizontal, the electric field was in the plane of the sample. Hence, the X-ray absorption near-edge structure spectroscopy (XANES) results are sensitive to the orbitals oriented parallel to the surface plane.[52] While self-absorption corrections are negligible due to the very low film thickness, all XRF and XANES data have been corrected for instrumental nonlinearities.[53]

2.4 *Ex situ* measurements

To study the growth mechanism of ZnO on the $In_{0.53}Ga_{0.47}As$ surface, we performed Atomic Force Microscopy (AFM) on a series of ZnO/$In_{0.53}Ga_{0.47}As$ samples grown at $T = 120$°C, using a Bruker Dimension Icon Atomic Force Microscope^{TM}. All ALD parameters were the same as those given above in section 2.2, except the total number of ALD cycles which varied from 5 to 50. Transmission electron microscopy (TEM) observations were carried out at 200 kV with a JEOL 2010 microscope (with a resolution of ~ 0.19 nm). Cross-sectioned samples were prepared by both manual and automated polishing, the latter using the MultiPrep^{TM} system (Allied High Tech

Products, Inc.). The final polishing was performed using a felt-covered disc impregnated with a silica solution until the appearance of the first extinction fringe among those of equal thickness. Ar-ion milling was then used to minimize the total thickness.

3 Results

3.1 XRF during growth

Figure 2(a) shows the evolution of Zn K_α fluorescence intensity as a function of the number of ALD cycles for $T_{substrate} = 120°C$. The overall XRF curve is not linear but exhibits an S-shape (sigmoidal) transition between two linear regions. The regions correspond to a low growth rate (cycles 1-25) and the steady, layer-by-layer growth above cycle $\sim$ 55. A close-up of the region between cycles 0 and 10 is shown in an inset by the green curve. As each ALD cycle begins with a DEZn pulse lasting 5 s, there is a jump in Zn fluorescence intensity at the start of each cycle. For cycles 1 to 27, the jump is followed by a decay that stems from the desorption of Zn (Zn atoms, Zn-containing molecules, DEZn molecules, and other products of the reaction) from the $In_{0.53}Ga_{0.47}As$ surface. The decay is absent at a higher number of cycles, and flat fluorescence intensity is observed after the DEZn injection (orange curve in Fig. 2 (a)).

To investigate the Zn desorption behavior, we fit the time dependence of the X-ray fluorescence using a linear combination of an exponential decay and a line. The results are shown in Fig. 2(b), where the dark blue fit curve is plotted on top of the light blue experimental curve. The difference between the Zn fluorescence intensity at the end of the DEZn pulse for each cycle n (black closed circles in Fig. 2(b)) and at the end of each full ALD cycle (red closed triangles) is displayed in the upper panel of Fig. 3 as a function of number of cycles. Note that the noise observed on the experimental curve is likely not only from the number of counts but also from the reproducibility of each ALD cycle. This involves the chemical reactions that take place on the surface, the flow of nitrogen between ALD pulses, and the pressure change inside the reactor chamber during the four different ALD steps. All of these factors impact the presence of DEZn molecules or Zn atoms

on the sample surface. Taking into account these possible variations, we find that Zn desorption no longer takes place or is minimized after ~ 28 ALD cycles. A cross-sectional TEM image of the sample after 25 cycles is shown in Fig. 4, it reveals the presence of a uniform, 1.3-nm-thick amorphous ZnO layer. This suggests that the end of Zn desorption is associated with complete coating of the $In_{0.53}Ga_{0.47}As$ surface. The transition between regions I and II of Fig. 3 marks a phenomenological change due to the fact that ZnO starts to grow on ZnO rather than on InGaAs, which leads to a change from 2D to 3D growth behavior.

As already noted, the evolution of Zn K_α fluorescence intensity in Fig. 2(a) is not a simple function of cycle number. We plot in the lower panel of Fig. 3 (filled triangles), the amount of growth per cycle, as measured by XRF (GPC(XRF)). These values correspond to the differences between the fit values, shown in Fig. 2, taken at the end of cycle n and $(n-1)$ and are plotted *vs* cycle n. For comparaison, we also plot the fluorescence growth per cycle obtained from the difference between the fit values, shown in Fig. 2, taken at the end of the DEZn pulse at cycle n and at the end of cycle $(n-1)$ (open circles). The curve represents the GPC as it would have been without the Zinc desorption. Beyond the region where desorption is detected (in region I), the experimental GPC(XRF) increases and reaches a maximum at cycle 38 before decreasing. This growth behavior is known as type II substrate-inhibited growth, which includes island growth, coalescence, and steady state growth[54], and is discussed further in sections 3.2 and 4.

3.2 Atomic force microscopy

We show in Fig. 5 2D AFM images of ZnO thin films grown on $In_{0.53}Ga_{0.47}As$ substrate for different number of cycles. 3D images are shown in Fig. S1 (Supplemental Information). The terrace height variation is shown by a change of color shade from darker (the minimum value is 0 nm - black) to lighter (the maximum value is 7 nm - white), with all images plotted according to the same height scale. A typical AFM image of the substrate surface after the 4M HCl etch step is shown in Fig. 5(a). The presence of steps and terraces on the surface of the $In_{0.53}Ga_{0.47}As$ substrate are clearly visible. The height of each step was systematically measured along a series

of parallel line-scans across the AFM images. A typical statistical distribution of step heights is shown in Fig. S2. As the $In_{1-x}Ga_xAs$ lattice parameter a can be determined by the Vegard's law, it depends on the ratio between the amounts of In and Ga atoms. In the case of $In_{0.53}Ga_{0.47}As$, the calculated lattice parameter (a) at room temperature is 0.586 nm, which is the same as that of InP. According to the experimental distribution of step heights in Fig. S2, the most likely value corresponds to a step height of one unit cell, a. The other three possible values are $0.5a$, $1.5a$ and $2a$. The root mean squared (RMS) surface roughness was determined for each individual terrace and averaged out of a series of RMS(AFM) measurements on several terraces. The RMS(AFM) values are shown in Fig. 6. Evidently, after 5 ALD cycles (Fig. 5 (b)), a faint, discontinuous deposit appears on the $In_{0.53}Ga_{0.47}As$ terraces, leading to a slight increase in RMS(AFM) surface roughness, as can be seen in Fig. 6. As more material is deposited, the terrace roughness continues to grow, and the presence of isolated platelets becomes more evident (Fig. 5 (c)). A percolated ultra-thin film forms after 15 cycles, as shown in Fig. 5(d). Holes are clearly visible at this stage (darker spots on the terraces). Eventually, the holes fill with more deposited material, and both the hole diameter (Fig. 5(e)) and terrace roughness (Fig. 6) decrease. A more uniform terraced surface can be seen in Fig. 5(e) at cycle 25.

After 25 cycles, 3D island growth begins: bright spots on a dark background are visible in Fig. 5(f) and (g). According to the XANES spectra (section 3.4), these bright spots may correspond to ZnO islands with a short-range order structure similar to that of wurtzite. Figure 5 (g) shows that for cycle 30, the average island size has increased, although there is still some variation in island shape and diameter. At cycle 50 (Fig. 5(i)), the surface is grainy with well-defined bright spots, indicating the formation of nanoparticles. The RMS(AFM) roughness appears to level off by cycle 50, as seen in Fig. 6. As has been pointed out in section 3.1, ZnO growth on $In_{0.53}Ga_{0.47}As$ can be divided into two stages: the first is characterized by a low and nearly constant growth rate concomitant with the detection of Zn desorption, and the second is characterized by island growth without any detectable Zn desorption. A smooth transition occurs between the two stages, as the first one is not finished before the second one starts. In the same way, the AFM images show that a

2D layer initially forms on the atomically flat $In_{0.53}Ga_{0.47}As$ terraces. Then, 3D ZnO island growth begins before total coalescence of the initial layer. The surface roughness increases as a function of ALD cycle number, with the gradual formation of ZnO nanoparticles.

3.3 Film mean thickness and growth rate

The thickness of the ZnO layers as a function of the number of cycles was investigated for three different substrate temperatures in the ALD window, $T_{substrate}$=100°C, 120°C, and 140°C. Every 5 ALD cycles up to cycle 50, a series of X-ray measurements (fluorescence and reflectivity) were conducted in 100 sccm of flowing N_2. The X-ray reflectivity curves are shown in the inset of Fig. 7. The data correspond to a substrate temperature of 120°C. The thickness fringes result from the different layer densities in the direction perpendicular to the sample surface, which include the growing ZnO layer, the 270-nm-thick $In_{0.53}Ga_{0.47}As$, and 10-nm-thick InP buffer layer on the InP crystal.

Fits to the XRR curves (inset of Fig. 7) allow determination of the ZnO mean thickness. However, as the ZnO layer is not continuous in the early stages of growth (section 3.2) or its thickness is so small (below 1-2 nm) that XRR oscillations are barely detected, the thickness could not determined below 30 cycles with such data. The dependence of the ZnO layer mean thickness μ on cycle number for different substrate temperatures is shown in Fig. 7. The trend of the Zn K_α fluorescence as a function of the number of cycles is similar to that of μ as the fluorescence intensity and the mean thickness are both proportional to the number of atoms per unit volume. Here, the experimental thickness value of the ZnO layer at cycle 50 (using both XRR and the TEM measurement) was used to calibrate the fluorescence intensity curves. The result, which now includes data for cycles 1-25, is shown in Fig. 8(a). With this information, the growth per cycle (GPC) can be found in a straightforward way by differentiating the thickness curve as a function of cycle number. Figure 8(b) shows the values of the derivative of the calibrated fluorescence curves.

The height and width of the GPC(XRF) peak vary for the different substrate temperatures $T_{substrate}$. The highest and the widest GPC(XRF) peak is observed for 120°C substrate temperature

curve. In addition, the experimental GPC(XRF) curve starts to rise earlier for $T_{substrate} = 120^{\circ}C$ (around 20 cycles) compared to the other substrate temperatures. Despite the differences between the GPC(XRF) curves, all three reach roughly the same value at cycle 50.

3.4 Fluorescence X-ray absorption near edge structure

Figure 9 shows the XANES spectra for different cycle numbers. They appear very similar in region I, regardless of the particular layer thickness. This suggests that the Zn chemical state and local environment do not change significantly up to cycle number 20. From the analysis presented in previous work,[55] we find that the XANES spectra reveal a disordered material with embryonic short-range order: the O nearest neighbors of Zn reside at the expected distances and angles for the wurtzite structure, at least within the sample plane. No out-of-plane short-range order is developed beyond the first shell in region I. During the transition to region II, new features appear on the XANES spectra (A, B, C, D, and E in Fig. 9), indicating that the Zn local environment begins to strongly resemble that of the wurtzite structure. According to the AFM images and GPC curves, these cycle numbers also correspond to the onset of 3D island growth, as described in section 3.3. However, TEM images and diffraction scans obtained at the end of region I, like the one shown in Fig. 4, show no evidence for long-range, crystalline order. This was observed also at the early stages of ZnO ALD on amorphous-SiO_2 at growth temperatures similar to those here.[45]

4 Island growth modeling

Non-linear ALD growth behavior has previously been analyzed using different phenomenological models.[56] Simulations of island growth by Monte Carlo techniques have also been demonstrated for amorphous[57] and polycrystalline films.[58,59] We have developed a quantitative, phenomenological model to describe the growth behavior observed in region II (Fig. 3), starting in the transition region when the coverage of the $In_{0.53}Ga_{0.47}As$ substrate with a 2D ZnO layer is about to be complete. It is based on an analytical model used to describe island growth by geometrical principles.[54]

We show that the different GPC curves obtained at the growth temperatures can be reproduced by slightly different pre-coalescence roughness values. In our model, we construct a square grid, each square with a side length of b. We then place hemispheroid nuclei at the centers of all the squares. According to this grid, the nearest distance between two nuclei centers is b. This implies that when the diameter of each hemispheroid island has increased to b, the islands start to coalesce. A cross section of an island is shown in Fig. 10.

We define r_0 and h_0 as the base radius and height of the island, respectively. If the ratio h/r is 1, the hemispheroid is a hemisphere. We assume that the radius r and height h increase by the values Δr and Δh, respectively, at each ALD cycle. Therefore $r = r_0 + n\Delta r$ and $h = h_0 + n\Delta h$, where n is the number of the ALD cycle.

We distinguish three growth phases depending on the ratio between the radius of the hemispheroidal base, r, and the distance between the islands, b, as shown in Fig. 11. **Phase I** corresponds to the growth of isolated islands ($r < b/2$) where the islands are well separated and not touching each other. As the radius r increases and reaches the value $r = b/2$, each island touches its four nearest neighbor islands. **Phase II** corresponds to island coalescence, when the radius r varies in the range $b/2 \leq r < b/\sqrt{2}$. During Phase II, the islands continue to coalesce until they completely cover the surface. This corresponds to the beginning of **Phase III**, where $r \geq b/\sqrt{2}$. The mean thickness μ (or equivalent layer thickness) of islands having the functional shape $z_{island}(x,y)$ and localized within a region D is defined as[54]

$$\mu = \frac{\int_D z_{island}(x,y)\,dxdy}{\int_D dxdy} \tag{1}$$

where x and y are in-plane coordinates. For the case of an isolated island with a volume $V(n)$, located in a square of area $b \times b$, the mean thickness at cycle n is

$$\mu(n) = \frac{V(n)}{b^2} \tag{2}$$

Using the model of hemipheroidal islands and knowing the functional shape of a surface covered with islands, $z(x,y)$, the RMS can be calculated at any cycle as follows:

$$RMS = \left[\frac{\int_D (z(x,y) - \mu)^2 dxdy}{\int_D dxdy} \right]^{1/2} . \quad (3)$$

We therefore distinguish four parameters affecting the growth of islands: $r_0[nm]$, $h_0[nm]$ – the hemispheroid initial radius and height, $\Delta r[nm]$ and $\Delta h[nm]$ – the incremental increase in radius and height per growth cycle, and $b[nm]$ – the average distance between the centers of the nearest neighbor islands.

Here we describe briefly the qualitative effects of these parameters. In Fig. 8(b), the GPC(XRF) curve exhibits a characteristic maximum. It corresponds to the cycle number for which the surface area of the film is at a maximum before the beginning of the next cycle. Generally, the cycle number of the peak maximum depends on the average distance between the centers of the nearest neighbor islands, b, on the initial size of the nuclei (r_0, h_0), and incremental values (Δr,Δh). In the simple case of hemispherical islands and $r_0 = h_0 = \Delta r = \Delta h$, it can be shown that during Phase I (Fig. 11(a)) the GPC is given by

$$GPC(n)_{Phase\,I} = \frac{\pi}{2} \Delta r \left(\frac{n - n_{inc}}{n_c} \right)^2 , \quad (4)$$

where n_c is the cycle number at which the islands starts to coalesce (Fig. 11(b)) and the GPC is close to a maximum. It can be directly determined/estimated from the experimental GPC curve. Knowing n_c and Δr, the nearest neighbor island distance is $b = 2n_c\Delta r$. We define n_{inc} as the cycle number immediately prior to the start of 3D island growth, i.e., at the onset of the change of slope of the experimental GPC curve concomitant with the onset of the Zn desorption decrease. During Phase III, as the radius of the islands continue to increase (Fig. 11(d)), the surface no longer roughens on average. When the total surface area becomes constant, the GPC vs. cycle function arrives at a plateau after the peak maximum. In this region, the GPC tends toward the value of Δh.

The experimental GPC(XRF) curves were fit in region II (Fig. 3), according to the growth model described above. In that region, we assume that Δr and Δh are constant and equal (i.e., that the growth is isotropic and the GPC$= \Delta r = \Delta h$). We define $(h/r)_{0.05}$ as the initial island aspect ratio at the onset of island growth that corresponds to a GPC close to 0.05 nm.cy^{-1}. Only $\Delta r = \Delta h$ and $(h/r)_{0.05}$ were allowed to vary. Region I, excep in the transition region, was excluded from our model since the incremental increase, $\Delta r = \Delta h$, is lower in region I due to Zn desorption, resulting in different growth behavior.

Determining the value of $\Delta r = \Delta h$ should be straightforward, as the experimental GPC(XRF) curve in Fig. 8 approaches it for a large number of cycles. However, our dataset is limited and does not arrive at a constant value after 50 cycles. But it was possible to obtain the experimental value of $\Delta r = \Delta h$ by fitting the GPC(XRF) curve at the left side of the GPC(XRF) maximum (Phase I) with equation 4, where n_c is a known experimental value. Then, the Δr and n_c values were used to simulate the entire GPC curve with the hemispherical island model, as described above.

Table 1: Best fit values of GPC$(= \Delta r = \Delta h)$ and $(\text{h/r})_{0.05}$ obtained for the modeling of the experimental GPC(XRF) curves shown in Fig. 12. T(°C) is the substrate temperature, GPC is the growth per cycle, $(\text{h/r})_{0.05}$ is the islands initial aspect ratio for GPC=0.05 nm.cy^{-1}. $\text{RMS}_{0.05}$ and RMS_{max} are the calculated root mean squared roughness values at GPC=0.05 nm.cy^{-1} and at the maximum of the GPC curve, respectively, $\sigma = 1/b^2$ is the islands density.

T(°C)	GPC, $nm.cy^{-1}$	$(\text{h/r})_{0.05}$	$\text{RMS}_{0.05}$ (nm)	RMS_{max} (nm)	σ $(10^{-2}\ nm^{-2})$
120	0.21	1.32	0.32	1.43	1.87
140	0.21	0.81	0.26	1.16	1.87
100	0.21	0.47	0.18	0.92	1.87

Figure 12 shows the experimental GPC(XRF) data at different substrate temperatures, $T_{\text{substrate}} = 100, 120, 140$°C (see Fig. 8), and the modeled GPC curves for region II. The inset of Fig. 12 shows the experimental GPC(XRF) data at $T_{\text{substrate}} = 120$°C, which corresponds to the GPC curve in Fig. 3 before calibration, and the modeled GPC curves. The results of modeling indicate that different slopes and peak heights of the GPC curve during Phase I, i.e., before coalescence, can be obtained with deviations in the $\Delta r = \Delta h$ values and/or pre-coalescence roughness (with larger roughness implying more surface available for growth). Different pre-coalescence roughnesses can

be achieved by varying the initial island aspect ratio (h/r) at the onset of island growth in Phase I (with the experimental GPC value being close to 0.05 nm.cy^{-1} in the present study). For instance, the inset of Fig. 12 shows the experimental GPC curve at $T_{\text{substrate}} = 120°$C (open circle) and calculated curves obtained with different initial island aspect ratios: $(\text{h/r})_{0.05}$ equal to one (blue solid line), greater than one (violet dotted-dashed line), and less than one (brown dashed line). Here, the GPC value was set to 0.19 nm.cy^{-1}. The effect of $(\text{h/r})_{0.05}$ on peak height is clearly visible. The best fit values of the GPC and initial island aspect ratios for the three GPC curves shown in Fig. 12, as well as the calculated root mean squared roughnesses and island densities, are given in Table 1. The GPC values are the same for the three temperature and equal to 0.21 nm.cy^{-1}, a value that compares well to the highest values found in the literature[60] and is close to that expected for ZnO wurtzite. Ideally, atomic layer deposition would give a GPC of 0.26 nm.cy^{-1}; experimentally, however, it is unlikely to reach such a value[50]. The different peak heights of the GPC curves is quite well reproduced with different initial island aspect ratios that are less than 1, less than but close to 1, and greater than one for $T_{\text{substrate}} = 100, 140, 120°$C, respectively. These simulations suggest that different pre-coalescence roughnesses during Phase I, stemming from the slightly different growth conditions, could result in variations of the GPC peak height, but the steady-state GPC value (at cycles > 55) remains the same.

The inset of Fig. 12 shows a representation of the GPC curve in region I by a sum of two functions: a slightly increasing straight line (until about cycle 20) and a sigmoidal function that goes to 0 above cycle 30 (black dotted-dashed line). The latter is very similar to the one shown in Fig. 3 (upper panel), i.e., it has the same width and is centered on the same cycle value. Interestingly, one can see that the modeled GPC curve (red dotted line) that is the sum of the GPC curves in region I (black dotted-dashed line) and II (blue solid line) perfectly fit the GPC experimental values in the transition region. Keeping in mind that the sigmoidal curve in Fig. 3 represents Zn desorption, this result further indicates that the transition region from the region I to region II is correlated with decreasing Zn desorption.

5 Discussion

We have demonstrated above that ZnO ALD on $In_{0.53}Ga_{0.47}As$ is characterized by an initial transient regime comprised of 2D growth and 3D islanding, followed by a steady-state growth regime with a growth rate of 0.21 nm.cy^{-1}.

In the case of oxide ALD with hydrogen transfer reactions and water used as an oxidant, one ALD cycle combines two self-terminating half reactions.[61,62] The first half reaction is the reaction of a metal precursor, ML_n, with an OH-terminated surface:

$$M-OH^{*}+ML_n \longrightarrow M-O-ML^{*}_{n-1}+HL \tag{5}$$

where M is the metal and L is the ligand. During the second half reaction, water replaces the adsorbed ligand with an OH-group:

$$ML^{*}+H_2O \longrightarrow M-OH^{*}+HL. \tag{6}$$

The probability of precursor adsorption and its chemical reaction directly affect the initial growth behavior.

It is known that there are several possible initial growth behaviors:[38] steady linear growth, substrate-enhanced growth, and substrate-inhibited growth. If the number of reactive sites on the bare substrate is higher or lower than on the ALD-grown material, either substrate-enhanced growth or substrate-inhibited growth, respectively, can occur. If the substrate surface is not highly reactive, growth occurs mainly on the more reactive areas. This leads to surface inhomogeneity and is the origin of substrate-inhibited growth behavior.[39] As the island size increases and growth enters the coalescence stage, a 2D layer is formed. If the ALD-grown material surface is fully covered by chemically reactive sites, steady linear growth behavior can begin.

A transient growth regime has already been reported for various materials grown by ALD. Elam *et al.*[40] used Auger electron spectroscopy to examine the initial stages of tungsten growth

on a SiO_2 substrate. They observed linear 2D growth for first few ALD cycles, but the growth rate was lower than for steady-state growth. The authors admit an equal probability of 2D and 3D growth behavior during the initial stage. Kim *et al.*[41] also showed that for Ru film deposition on TiN and SiO_2, the transient region was present. Growth was inhibited for first several ALD cycles due to the weak interaction between the Ru precursor and the covalent bonds in TiN and SiO_2. Furthermore, for the same material deposited on different substrates, the incubation time can vary or be absent entirely. Lim *et al.*[42] showed, using a simple analytical kinetic model, that at the beginning of growth a transient regime exists until the deposited material fully covers the substrate surface; only then can steady linear growth take place. Thus, the incubation time could correspond to the time necessary to cover the total substrate surface. Satta *et al.*[43] investigated TiO_2 surface coverage on SiO_2 substrates as a function of the number of deposition cycles. They demonstrated a slow, linear increase of surface coverage in the first stage of growth due to a non-reactive surface. Then, since the probability of adsorption varies on a mixed surface, this led to 3D island growth. Deposition eventually entered a steady linear growth regime. Green *et al.*[44] observed similar growth behavior for HfO_2 on Si substrates. The Si substrate surface was oxidized by different ways, and the authors showed that a thin oxide layer (less than 1 nm) changes the properties of the sample surface, impacting the initial growth stage. They also found that the probability of starting a chemical reaction is higher when the SiO_x surface is terminated with OH-groups.

In the present study, we have evidenced a transient regime that we divide into two steps (regions I and II, as indicated in Fig. 3). Region I corresponds to a regime in which Zn-containing molecules desorb from the surface, as detected by XRF. Here, the growth rate is very low (< 0.05 nm/cycle) and nearly constant, as long as the Zn desorption magnitude is about the same. A transition stage then takes place, and the GPC starts to increase as the amount desorbed decreases (Fig. 3). Region II is characterized by the absence of precursor desorption and a rapid change in growth rate, as described in sections 3.2 and 4. Note that only chemically adsorbed DEZn precursor or Zn-containing molecules are detected in our experiments, since physically adsorbed molecules can be easily removed during the N_2 purging step.[37,63] As was shown in Fig. 3, there is no evidence of Zn

desorption after 28 ALD cycles.

In the region I, the low and nearly constant growth rate (GPC) is associated with the inertness of the substrate surface and a nearly constant sticking coefficient. This is likely to be associated with a low density of active sites (e.g., OH groups)[44,64,65] which hampers precursor (DEZn) and reactant (H_2O) chemisorption. During the oxidant pulse, water reacts with the sample surface and leaves active sites for reaction with DEZn; these chemical reactions are given by equations 5 and 6. Indeed, we show in Fig. S3 (Supplemental Information) that increasing the water flow shortens the delay in ZnO nucleation, most likely due to increased active site density on the $In_{0.53}Ga_{0.47}As$ surface. Interestingly, as observed in Fig. 12, the amount of Zn deposited after the first cycle is about three times higher than the following few cycles, and there is almost no desorption. This indicates that surface functionalization changes after the first cycle whereas it does not for the subsequent cycles (until ZnO no longer desorbs). A close inspection of the AFM images strongly suggests that the fading of the desorption stage is correlated with the closure of a 2D layer, which is concomitant with the onset of 3D ZnO islands (corresponding to the transition stage in Fig. 3). Figure 3 shows that in region I, the Zn desorption amount stays constant for each cycle despite the fact that the $In_{0.53}Ga_{0.47}As$ and ZnO surface fractions vary during growth. This suggests that the Zn and oxygen atoms incorporate preferentially at the edge of the platelets.

All of these XRF and AFM observations indicate that growth in region I consists of a period of incubation with low growth rate, during which the substrate surface transforms its functional groups and results in the fabrication of a 2D layer.[43] A 2D-like mechanism of growth distinguishes this phase.

Region II is characterized by an absence of precursor desorption and ZnO island growth. As shown in Fig. 3, beyond cycle 25, the ZnO islands start to grow on the surface of the 2D ZnO layer. The AFM images (Fig. 5 (f-i)) provide evidence for a high density of islands with a rather large size distribution, such that it is difficult to distinguish well-separated islands. However, it is clear that the average island diameter increases as a function of ALD cycle number. Furthermore, island growth is accompanied by a change in the surface roughness (Fig. 6). Accordingly, the mean

thickness curves (Fig. 8(a)) show the typical S-shape in region II associated with 3D island growth and coalescence.[54,56]

The formation of a 2D ZnO layer on the $In_{0.53}Ga_{0.47}As$ surface followed by 3D ZnO island growth is sketched in Fig. 13. First, the $In_{0.53}Ga_{0.47}As$ surface (Fig. 13(a)) starts to be covered with platelets (Fig. 13(b, c)), and the sample surface roughness increases. Right before completion of the 2D ZnO layer, holes are visible at the surface (Fig. 13(d)), which then shrink (Fig. 13(e)). The TEM image reveals that the 2D layer is amorphous (Fig. 4). The XANES spectra (Fig. 9) confirm that the atomic structure of the 2D Zn-oxide layer is disordered but has an embryonic wurtzite structure. ZnO island growth starts on top of the 2D ZnO layer (Fig. 13(f)), and the growth rate (GPC) reaches a constant value after the transient regime, as seen during substrate-inhibited growth.

The simple growth model proposed in section 4 allows us to analyze the GPC curves. The simulations suggest that different pre-coalescence roughnesses during Phase I could result in variations of the GPC peak height, while the steady-state GPC value (at cycles > 55) remains the same, as is the case for the three GPC(XRF) curves reported in Fig. 8 (b). The lowest roughness in the transient regime, notably at the maximum of GPC curves, is achieved for the lowest temperature. The GPC values are about the same and equal to 0.21 $nm.cy^{-1}$ for the three substrate temperatures (100°C, 120°C and 140°C). This is in agreement with the fact that these three temperature values are all within the ALD temperature window.

6 Conclusion

We have performed the first detailed study on the evolution of the growth process during the initial stages of ZnO growth on $In_{0.53}Ga_{0.47}As$ by ALD. It was demonstrated that growth passes through a transient stage before the onset of steady-state growth. The transient stage is comprised of two regimes separated by a transition stage. Using *in situ* synchrotron X-ray fluorescence, reflectivity, and absorption spectroscopy, we have demonstrated that the first regime of growth (up to 28 cycles,

region I) is far from ideal ALD growth. During this regime, we find that the substrate-inhibited ZnO growth mode takes place on InGaAs terraces. It results in a slow growth rate (¡ 0.05 nm.cy^{-1}) with the desorption of molecules containing Zn. This leads eventually to the formation of a $\sim$1-nm-thick 2D amorphous ZnO layer (at about cycle 25). By the end of the first regime (region I), a transition occurs in which the GPC starts to increase when the amount of desorption decreases, and growth enters into a second regime (region II). The phenomenological model we developed to describe the change of GPC behavior suggests 3D island formation in region II, with an island aspect ratio, i.e. initial surface roughness, that depends on the growth condition. The transient regime (regions I and II) ends with island coalescence. The growth is finally characterized by a steady growth rate of 0.21 nm.cy^{-1}, as expected for layer-by-layer ZnO ALD. This shows that ideal ALD behavior is not always achievable, especially at the initial stages of heterogeneous growth.

Our work demonstrates the unique power of *in situ* synchrotron methods for elucidating the atomistic processes taking place during the initial stages of ALD. We find that the complementary suite of tools used here is key to optimizing the growth process and material quality. Furthermore, the successful growth of a 1-nm-thick 2D ZnO layer is highly encouraging for the future development of ZnO IPLs and III-V surface passivation.

Acknowledgement

E.S. was supported by the LabEx Minos ANR-10-LABX-55-01. Financial support for this work by ANR Moon (ANR-11-NANO-0014) is gratefully acknowledged. D.D.F. was supported by both an award from the Nanosciences Foundation and the U.S. Department of Energy, Office of Science, Office of Basic Energy Sciences, Materials Sciences and Engineering Division. We acknowledge D. De Barros for the engineering assistance. We thank Synchrotron SOLEIL for general facilities placed at our disposal, and in particular, N. Aubert for his help with the experimental setup. The experiment at the SIRIUS beamline benefited from the SOLEIL beam time allocation No. 2015613.

Supporting Information Available

3D AFM images of ZnO layers on $In_{0.53}Ga_{0.47}As$ terraces, statistical distribution of step heights on cleaned $In_{0.53}Ga_{0.47}As$ surface and the effect of increasing the water flow on the delay of ZnO nucleation, are provided in the Supplemental Information. This material is available free of charge via the Internet at http://pubs.acs.org/.

References

(1) Schaller, R. R. Moore's law: past, present and future. *IEEE spectrum* **1997**, *34*, 52–59.

(2) Del Alamo, J. A. Nanometre-scale electronics with III-V compound semiconductors. *Nature* **2011**, *479*, 317–323.

(3) Heyns, M.; Tsai, W. Ultimate scaling of CMOS logic devices with Ge and III–V materials. *Mrs bulletin* **2009**, *34*, 485–492.

(4) Fang, H.; Madsen, M.; Carraro, C.; Takei, K.; Kim, H. S.; Plis, E.; Chen, S.-Y.; Krishna, S.; Chueh, Y.-L.; Maboudian, R.; Javey, A. Strain engineering of epitaxially transferred, ultrathin layers of III-V semiconductor on insulator. *Applied Physics Letters* **2011**, *98*, 012111.

(5) Paladugu, M.; Merckling, C.; Loo, R.; Richard, O.; Bender, H.; Dekoster, J.; Vandervorst, W.; Caymax, M.; Heyns, M. Site selective integration of III–V materials on Si for nanoscale logic and photonic devices. *Crystal Growth & Design* **2012**, *12*, 4696–4702.

(6) Sonnet, A. M.; Galatage, R. V.; Hurley, P. K.; Pelucchi, E.; Thomas, K.; Gocalinska, A.; Huang, J.; Goel, N.; Bersuker, G.; Kirk, W. P.; Hinkle, C. L.; Vogel, E. M. Remote phonon and surface roughness limited universal electron mobility of $In_{0.53}Ga_{0.47}As$ surface channel MOSFETs. *Microelectronic Engineering* **2011**, *88*, 1083 – 1086.

(7) Ishii, H.; Miyata, N.; Urabe, Y.; Itatani, T.; Yasuda, T.; Yamada, H.; Fukuhara, N.; Hata, M.; Deura, M.; Sugiyama, M.; Takenaka, M.; Takagi, S. High Electron Mobility Metal-Insulator-

Semiconductor Field-Effect Transistors Fabricated on (111)-Oriented InGaAs Channels. *Applied Physics Express* **2009**, *2*, 121101.

(8) Takagi, S.; Noguchi, M.; Kim, M.; Kim, S.-H.; Chang, C.-Y.; Yokoyama, M.; Nishi, K.; Zhang, R.; Ke, M.; Takenaka, M. III-V/Ge MOS device technologies for low power integrated systems. *Solid-State Electronics* **2016**, *125*, 82–102.

(9) Oktyabrsky, S., Ye, P., Eds. *Fundamentals of III-V Semiconductor MOSFETs*; Springer US: Boston, MA, 2010; DOI: 10.1007/978-1-4419-1547-4.

(10) Woolley, J. C.; Thomas, M. B.; Thompson, A. G. Optical energy gap variation in $Ga_xIn_{1-x}As$ alloys. *Canadian Journal of Physics* **1968**, *46*, 157–159.

(11) Wagner, J. W. Preparation and Properties of Bulk $In_{1-x}Ga_xAs$ Alloys. *Journal of The Electrochemical Society* **1970**, *117*, 1193–1196.

(12) Kumar, A.; Bose, D. Compound Semiconductor Photodetectors: A Review. *IETE Journal of Research* **1997**, *43*, 257–265.

(13) Hall, D.; Liu, Y.-H.; Lo, Y.-H. Single photon avalanche detectors: prospects of new quenching and gain mechanisms. *Nanophotonics* **2015**, *4*, 397–412.

(14) Wang, C.; Ke, S.; Hu, W.; Yang, J.; Yang, Y. Review of Quantum Dot-in-a-Well Infrared Photodetectors and Prospect of New Structures. *Journal of Nanoscience and Nanotechnology* **2016**, *16*, 8046–8054.

(15) Diehl, R. *High-power diode lasers: fundamentals, technology, applications*; Springer Science & Business Media, 2003; Vol. 78.

(16) Bennett, B. R.; Magno, R.; Boos, J. B.; Kruppa, W.; Ancona, M. G. Antimonide-based compound semiconductors for electronic devices: A review. *Solid-State Electronics* **2005**, *49*, 1875–1895.

(17) Ajayan, J.; Nirmal, D. A review of InP/InAlAs/InGaAs based transistors for high frequency applications. *Superlattices and Microstructures* **2015**, *86*, 1–19.

(18) Agrawal, A.; Shukla, N.; Ahmed, K.; Datta, S. A unified model for insulator selection to form ultra-low resistivity metal-insulator-semiconductor contacts to n-Si, n-Ge, and n-InGaAs. *Applied Physics Letters* **2012**, *101*, 042108.

(19) George, S. M. Atomic layer deposition: an overview. *Chem. Rev* **2010**, *110*, 111–131.

(20) Wallace, R. M.; McIntyre, P. C.; Kim, J.; Nishi, Y. Atomic layer deposition of dielectrics on Ge and III–V materials for ultrahigh performance transistors. *MRS bulletin* **2009**, *34*, 493–503.

(21) Ye, P.; Wilk, G.; Yang, B.; Kwo, J.; Gossmann, H.-J.; Hong, M.; Ng, K.; Bude, J. Depletion-mode InGaAs metal-oxide-semiconductor field-effect transistor with oxide gate dielectric grown by atomic-layer deposition. *Applied Physics Letters* **2004**, *84*, 434–436.

(22) Xuan, Y.; Wu, Y.; Lin, H.; Shen, T.; Peide, D. Y. Submicrometer Inversion-Type Enhancement-Mode InGaAs MOSFET With Atomic-Layer-Deposited Al_2O_3 as Gate Dielectric. *IEEE Electron Device Letters* **2007**, *28*, 935–938.

(23) Xuan, Y.; Wu, Y.; Shen, T.; Yang, T.; Ye, P. High performance submicron inversion-type enhancement-mode InGaAs MOSFETs with ALD Al_2O_3, HfO_2 and HfAlO as gate dielectrics. Electron Devices Meeting, 2007. IEDM 2007. IEEE International. 2007; pp 637–640.

(24) Lee, K.; Lee, Y.; Chang, P.; Huang, M.; Chang, Y.; Hong, M.; Kwo, J. Achieving 1 nm capacitive effective thickness in atomic layer deposited HfO_2 on $In_{0.53}Ga_{0.47}As$. *Applied Physics Letters* **2008**, *92*, 252908.

(25) Chang, C.-H.; Chiou, Y.-K.; Chang, Y.-C.; Lee, K.-Y.; Lin, T.-D.; Wu, T.-B.; Hong, M.;

Kwo, J. Interfacial self-cleaning in atomic layer deposition of Hf O 2 gate dielectric on In 0.15 Ga 0.85 As. *Applied physics letters* **2006**, *89*, 242911.

(26) Goel, N.; Majhi, P.; Chui, C.; Tsai, W.; Choi, D.; Harris, J. InGaAs metal-oxide-semiconductor capacitors with Hf O 2 gate dielectric grown by atomic-layer deposition. *Applied physics letters* **2006**, *89*, 163517.

(27) Huang, M.; Chang, Y.; Chang, Y.; Lin, T.; Kwo, J.; Hong, M. Energy-band parameters of atomic layer deposited Al 2 O 3 and HfO 2 on In x Ga 1- x As. *Applied Physics Letters* **2009**, *94*, 052106.

(28) Aguirre-Tostado, F.; Milojevic, M.; Lee, B.; Kim, J.; Wallace, R. In situ study of surface reactions of atomic layer deposited La x Al 2- x O 3 films on atomically clean In 0.2 Ga 0.8 As. *Applied Physics Letters* **2008**, *93*, 172907.

(29) Park, M.-S.; Razaei, M.; Barnhart, K.; Tan, C. L.; Mohseni, H. Surface passivation and aging of InGaAs/InP heterojunction phototransistors. *Journal of Applied Physics* **2017**, *121*, 233105.

(30) Ameen, M.; Nyns, L.; Sioncke, S.; Lin, D.; Ivanov, T.; Conard, T.; Meersschaut, J.; Feteha, M.; Van Elshocht, S.; Delabie, A. Al2O3/InGaAs metal-oxide-semiconductor interface properties: Impact of Gd2O3 and Sc2O3 interfacial layers by atomic layer deposition. *ECS Journal of Solid State Science and Technology* **2014**, *3*, N133–N141.

(31) Chang, C.-Y.; Ichikawa, O.; Osada, T.; Hata, M.; Yamada, H.; Takenaka, M.; Takagi, S. Impact of La2O3 interfacial layers on InGaAs metal-oxide-semiconductor interface properties in Al2O3/La2O3/InGaAs gate stacks deposited by atomic-layer-deposition. *Journal of Applied Physics* **2015**, *118*, 085309.

(32) He, G.; Gao, J.; Chen, H.; Cui, J.; Sun, Z.; Chen, X. Modulating the interface quality and electrical properties of HfTiO/InGaAs gate stack by atomic-layer-deposition-derived Al2O3 passivation layer. *ACS applied materials & interfaces* **2014**, *6*, 22013–22025.

(33) Kim, S. H.; Joo, S. Y.; Jin, H. S.; Kim, W.-B.; Park, T. J. Ultrathin ZnS and ZnO Interfacial Passivation Layers for Atomic-Layer-Deposited HfO2 Films on InP Substrates. *ACS applied materials & interfaces* **2016**, *8*, 20880–20884.

(34) Chen, L.; Yu-Ming, Z.; Yi-Men, Z.; Hong-Liang, L. Interfacial characteristics of Al/Al2O3/ZnO/n-GaAs MOS capacitor. *Chinese Physics B* **2013**, *22*, 076701.

(35) Liao, M.-H.; Chen, P.-K. Experimental demonstration on the ultra-low source/drain resistance by metal-insulator-semiconductor contact structure in In0. 53Ga0. 47As field-effect transistors. *AIP Advances* **2013**, *3*, 092118.

(36) Liao, M.-H.; Lien, C. The comprehensive study and the reduction of contact resistivity on the n-InGaAs MIS contact system with different inserted insulators. *AIP Advances* **2015**, *5*, 057117.

(37) Puurunen, R. L. Surface chemistry of atomic layer deposition: A case study for the trimethylaluminum/water process. *Journal of applied physics* **2005**, *97*, 9.

(38) Puurunen, R. L.; Vandervorst, W. Island growth as a growth mode in atomic layer deposition: A phenomenological model. *Journal of Applied Physics* **2004**, *96*, 7686–7695.

(39) Baji, Z.; Labadi, Z.; Horvath, Z. E.; Molnar, G.; Volk, J.; Barsony, I.; Barna, P. Nucleation and growth modes of ALD ZnO. *Crystal Growth & design* **2012**, *12*, 5615–5620.

(40) Elam, J.; Nelson, C.; Grubbs, R.; George, S. Nucleation and growth during tungsten atomic layer deposition on SiO 2 surfaces. *Thin Solid Films* **2001**, *386*, 41–52.

(41) Kim, S. K.; Han, J. H.; Kim, G. H.; Hwang, C. S. Investigation on the growth initiation of Ru thin films by atomic layer deposition. *Chemistry of Materials* **2010**, *22*, 2850–2856.

(42) Lim, J.-W.; Park, H.-S.; Kang, S.-W. Analysis of a transient region during the initial stage of atomic layer deposition. *Journal of Applied Physics* **2000**, *88*, 6327–6331.

(43) Satta, A.; Schuhmacher, J.; Whelan, C. M.; Vandervorst, W.; Brongersma, S. H.; Beyer, G. P.; Maex, K.; Vantomme, A.; Viitanen, M. M.; Brongersma, H. H.; Besling, W. F. A. Growth mechanism and continuity of atomic layer deposited TiN films on thermal SiO2. *Journal of Applied Physics* **2002**, *92*, 7641–7646.

(44) Green, M. L.; Ho, M.-Y.; Busch, B.; Wilk, G. D.; Sorsch, T.; Conard, T.; Brijs, B.; Vandervorst, W.; Risnen, P. I.; Muller, D.; Bude, M.; Grazul, J. Nucleation and growth of atomic layer deposited HfO2 gate dielectric layers on chemical oxide (SiOH) and thermal oxide (SiO2 or SiON) underlayers. *Journal of Applied Physics* **2002**, *92*, 7168–7174.

(45) Fong, D.; Eastman, J.; Kim, S.; Fister, T.; Highland, M.; Baldo, P.; Fuoss, P. In situ synchrotron x-ray characterization of ZnO atomic layer deposition. *Applied Physics Letters* **2010**, *97*, 191904.

(46) Klug, J. A.; Weimer, M. S.; Emery, J. D.; Yanguas-Gil, A.; Seifert, S.; Schlepütz, C. M.; Martinson, A. B.; Elam, J. W.; Hock, A. S.; Proslier, T. A modular reactor design for in situ synchrotron x-ray investigation of atomic layer deposition processes. *Review of Scientific Instruments* **2015**, *86*, 113901.

(47) Dendooven, J.; Solano, E.; Minjauw, M. M.; Van de Kerckhove, K.; Coati, A.; Fonda, E.; Portale, G.; Garreau, Y.; Detavernier, C. Mobile setup for synchrotron based in situ characterization during thermal and plasma-enhanced atomic layer deposition. *Review of Scientific Instruments* **2016**, *87*, 113905.

(48) Sun, Y.; Pianetta, P.; Chen, P.-T.; Kobayashi, M.; Nishi, Y.; Goel, N.; Garner, M.; Tsai, W. Arsenic-dominated chemistry in the acid cleaning of InGaAs and InAlAs surfaces. *Applied Physics Letters* **2008**, *93*, 194103.

(49) Boichot, R. et al. Evolution of Crystal Structure During the Initial Stages of ZnO Atomic Layer Deposition. *Chem. Mater.* **2016**, *28*, 592–600.

(50) Gao, Z.; Wu, F.; Myung, Y.; Fei, R.; Kanjolia, R.; Yang, L.; Banerjee, P. Standing and sitting adlayers in atomic layer deposition of ZnO. *Journal of Vacuum Science & Technology A: Vacuum, Surfaces, and Films* **2016**, *34*, 01A143.

(51) Ciatto, G.; Chu, M.; Fontaine, P.; Aubert, N.; Renevier, H.; Deschanvres, J. SIRIUS: A new beamline for in situ X-ray diffraction and spectroscopy studies of advanced materials and nanostructures at the SOLEIL Synchrotron. *Thin Solid Films* **2016**, *617*, 48–54.

(52) Brouder, C. Angular dependence of X-ray absorption spectra. *Journal of Physics: Condensed Matter* **1990**, *2*, 701.

(53) Ciatto, G.; d'Acapito, F.; Boscherini, F.; Mobilio, S. Treatment of EXAFS data taken in the fluorescence mode in non-linear conditions. *Journal of synchrotron radiation* **2004**, *11*, 278–283.

(54) Nilsen, O.; Mohn, C.; Kjekshus, A.; Fjellvåg, H. Analytical model for island growth in atomic layer deposition using geometrical principles. *Journal of Applied Physics* **2007**, *102*, 024906.

(55) Chu, M. H.; Tian, L.; Chaker, A.; Cantelli, V.; Ouled, T.; Boichot, R.; Crisci, A.; Lay, S.; Richard, M.-I.; Thomas, O.; Deschanvres, J.-L.; Renevier, H.; Fong, D. D.; Ciatto, G. An Atomistic View of the Incipient Growth of Zinc Oxide Nanolayers. *Crystal Growth & Design* **2016**, *16*, 5339–5348.

(56) Puurunen, R. L.; Vandervorst, W. Island growth as a growth mode in atomic layer deposition: A phenomenological model. *Journal of Applied Physics* **2004**, *96*, 7686–7695.

(57) Nilsen, O.; Karlsen, O. B.; Kjekshus, A.; Fjellvåg, H. Simulation of growth dynamics in atomic layer deposition. Part I. Amorphous films. *Thin Solid Films* **2007**, *515*, 4527–4537.

(58) Nilsen, O.; Karlsen, O. B.; Kjekshus, A.; Fjellvåg, H. Simulation of growth dynamics in atomic layer deposition. Part II. Polycrystalline films from cubic crystallites. *Thin Solid Films* **2007**, *515*, 4538–4549.

(59) Nilsen, O.; Karlsen, O. B.; Kjekshus, A.; Fjellvåg, H. Simulation of growth dynamics in atomic layer deposition. Part III. Polycrystalline films from tetragonal crystallites. *Thin Solid Films* **2007**, *515*, 4550–4558.

(60) Tynell, T.; Karppinen, M. Atomic layer deposition of ZnO: a review. *Semiconductor Science and Technology* **2014**, *29*, 043001.

(61) Hwang, C. S. *Atomic layer deposition for semiconductors*; Springer, 2013.

(62) Puurunen, R. L. et al. Island growth in the atomic layer deposition of zirconium oxide and aluminum oxide on hydrogen-terminated silicon: Growth mode modeling and transmission electron microscopy. *Journal of Applied Physics* **2004**, *96*, 4878–4889.

(63) Yim, S.-S.; Lee, D.-J.; Kim, K.-S.; Kim, S.-H.; Yoon, T.-S.; Kim, K.-B. Nucleation kinetics of Ru on silicon oxide and silicon nitride surfaces deposited by atomic layer deposition. *Journal of Applied Physics* **2008**, *103*, 113509.

(64) Puurunen, R. L. Correlation between the growth-per-cycle and the surface hydroxyl group concentration in the atomic layer deposition of aluminum oxide from trimethylaluminum and water. *Applied surface science* **2005**, *245*, 6–10.

(65) Tapily, K.; Gu, D.; Baumgart, H. Growth Mechanism of ALD ZnO Films Investigated by Physical Characterization. *ECS Transactions* **2010**, *33*, 355–363.

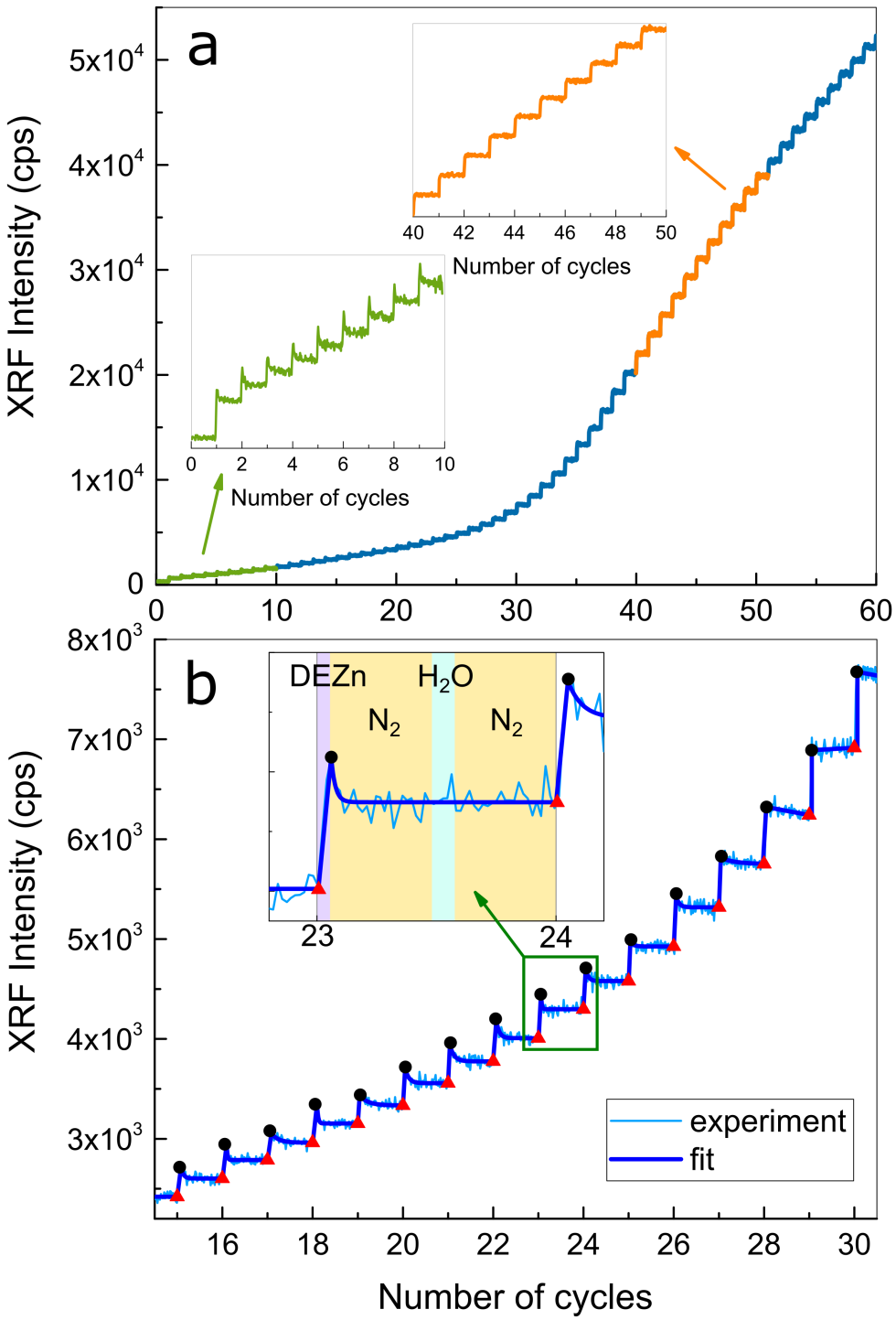

Figure 2: (a) Zn K_α X-ray fluorescence intensity ($T_{substrate} = 120°C$) vs. cycle number. The insets show the Zn fluorescence intensity (green curve) at the early stages, as compared with intensity at the later stages (orange curve). (b) The experimental Zn fluorescence intensity (light blue curve) and fit (dark blue curve) for cycles 15-30. The inset shows the fluorescence intensity and fit curve for cycle 24. Black closed circles indicate the Zn fluorescence intensity at the end of the DEZn pulse, and red closed triangles indicate the Zn fluorescence intensity at the end of each ALD cycle.

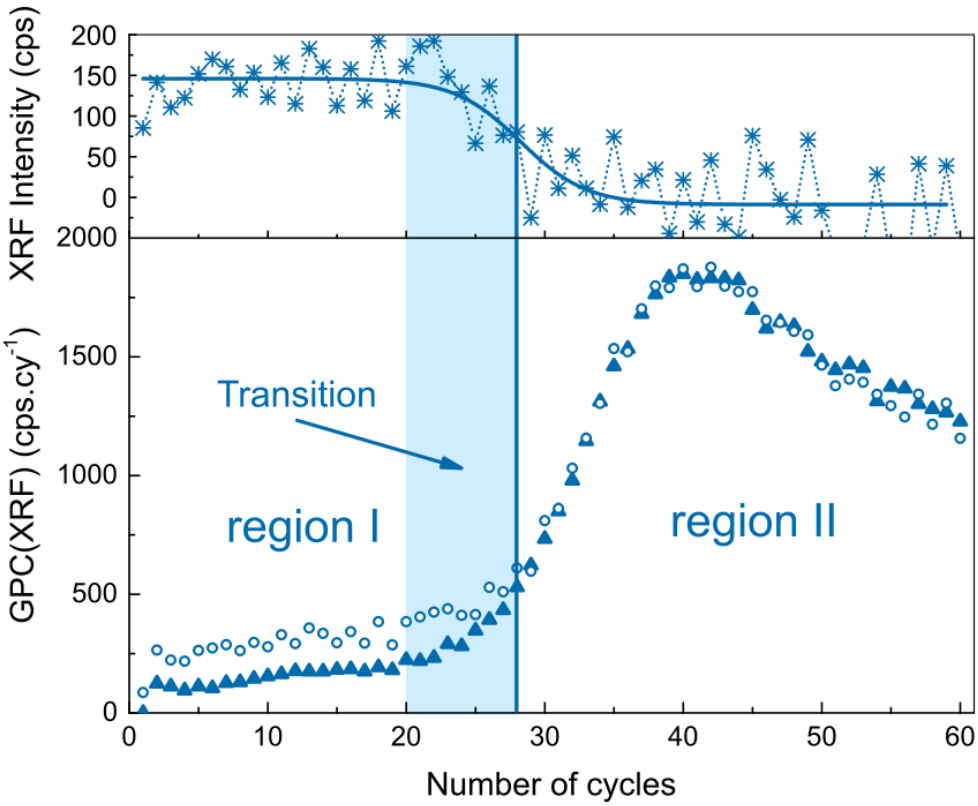

Figure 3: Upper panel. Difference between the Zn fluorescence intensity fit values, shown in Fig. 2, taken at the end of the Zn pulse and at the end of each cycle, as a function of number of cycles ($T_{substrate} = 120°C$). The fit curve is a sigmoidal function. Lower panel. Triangles: Fluorescence growth per cycle (GPC) obtained from the difference between the fit values, shown in Fig. 2, taken at the end of cycles n and $(n-1)$ *vs* cycle n, values ($T_{substrate} = 120°$C). Open circles: fluorescence growth per cycle obtained from the difference between the fit values, shown in Fig. 2, taken at the end of the DEZn pulse at cycle n and at the end of cycle $(n-1)$. Region I corresponds to the detection by XRF of desorbed molecules containing Zn. A transition region is observed when going from region I to region II.

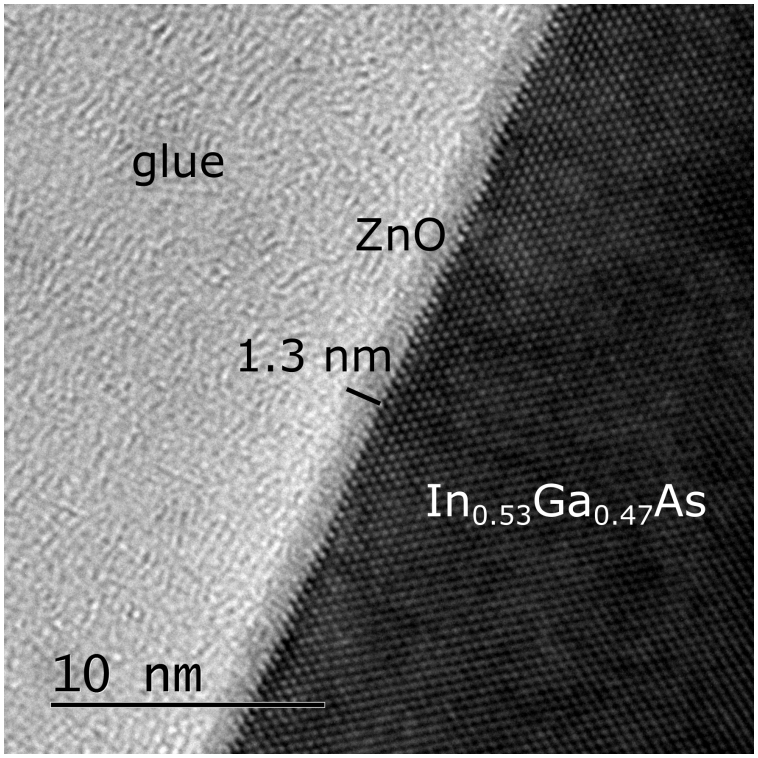

Figure 4: TEM cross-sectional image of a ZnO layer on $In_{0.53}Ga_{0.47}As$ obtained after 25 ALD cycles ($T_{substrate} = 120°C$).

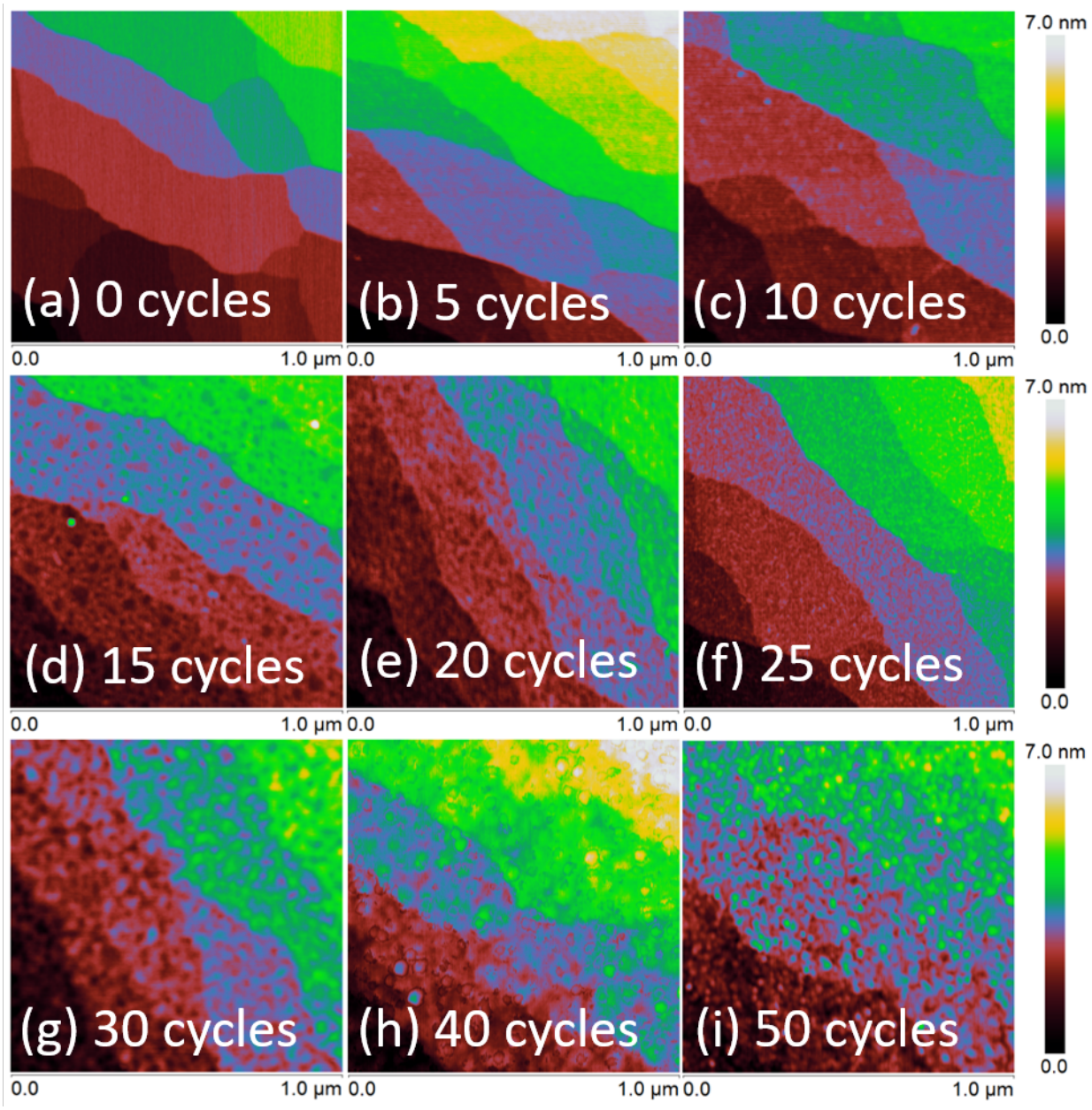

Figure 5: Post growth AFM images of ZnO films grown on $In_{0.53}Ga_{0.47}As$ for different number of cycles: 0 (a), 5 (b), 10 (c), 15 (d), 20 (e), 25 (f), 30 (g), 40 (h) and 50 (i). A 3D rendering of the same images is shown in Fig. S1.

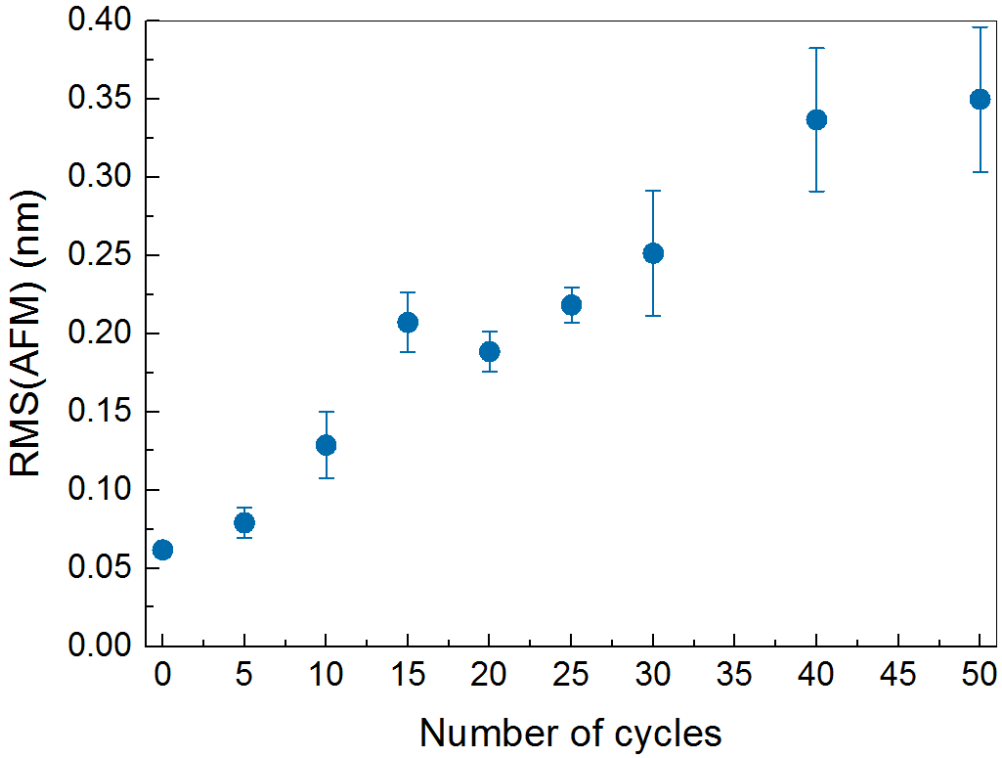

Figure 6: RMS(AFM) roughness of the $In_{0.53}Ga_{0.47}As$ terraces as a function of ALD cycle number. The AFM-determined values were calculated by averaging different RMS(AFM) roughnesses obtained on several terraces. Note that the RMS represents surface height variations with a lateral scale of the order of 20-50 nm.

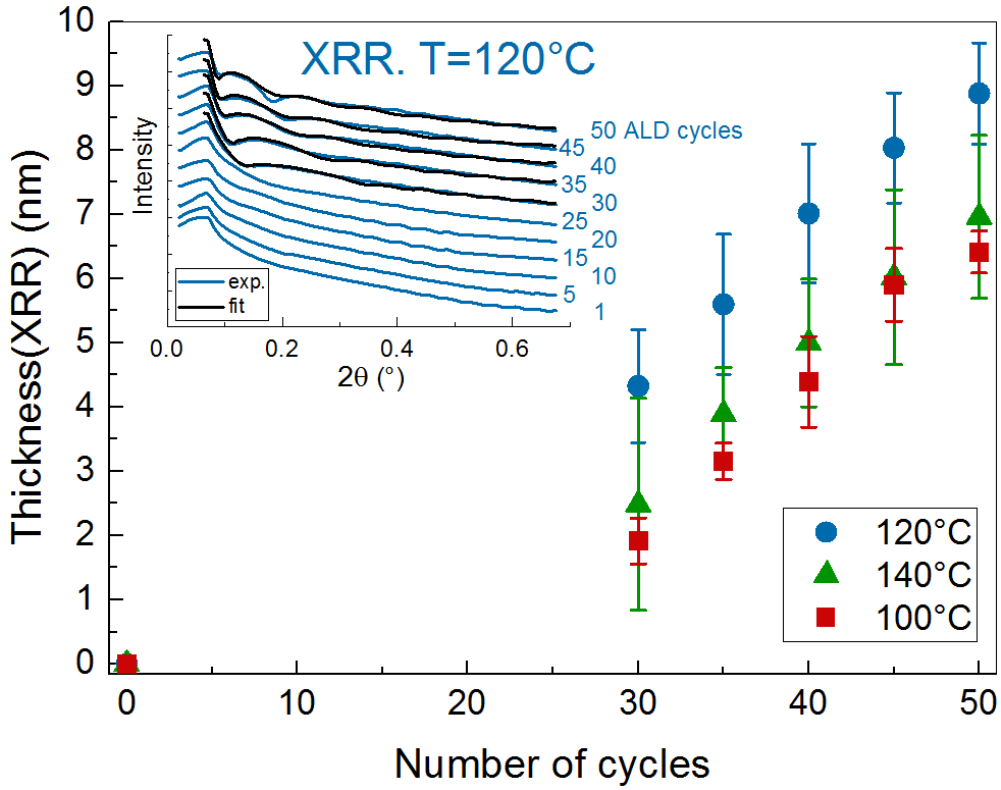

Figure 7: ZnO layer thickness as a function of the ALD cycle number for a substrate temperature equal to 100°C, 120°C and 140°C, extracted from X-ray reflectivity curves measured during growth every 5 cycles in N_2 flow. Inset: XRR experimental (blue lines) and fit (black lines) curves as a function of ALD cycle number for a substrate temperature, $T_{substrate} = 120°C$.

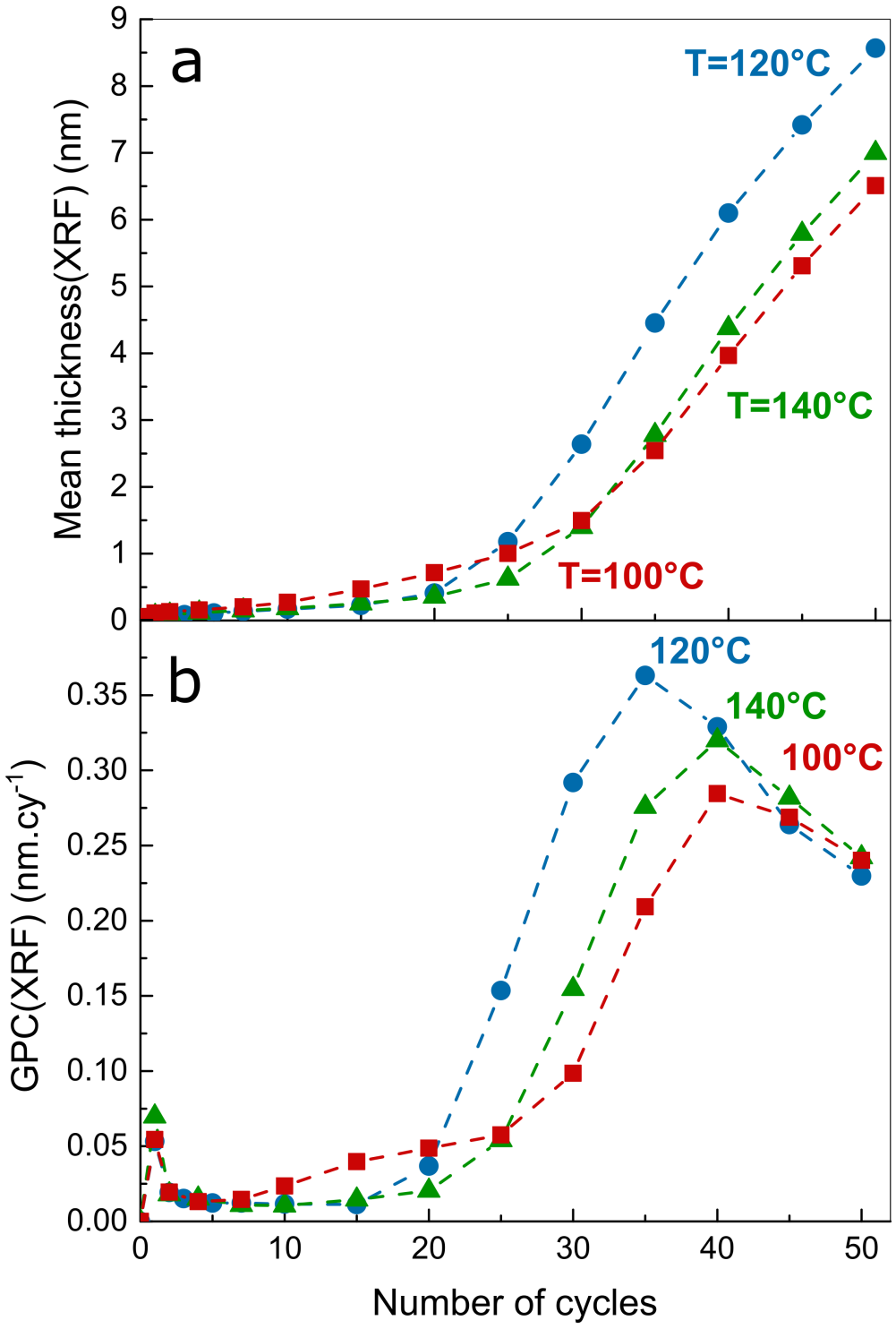

Figure 8: (a) ZnO layer (film) mean thickness as a function of cycle number for three different $In_{0.53}Ga_{0.47}As$ substrate temperatures; Zn K_α fluorescence intensities were calibrated with XRR measurements. (b) Experimental ZnO film mean growth GPC(XRF). The X-ray fluorescence (XRF) data were recorded after the completion of ALD cycles (which took place without X-rays).

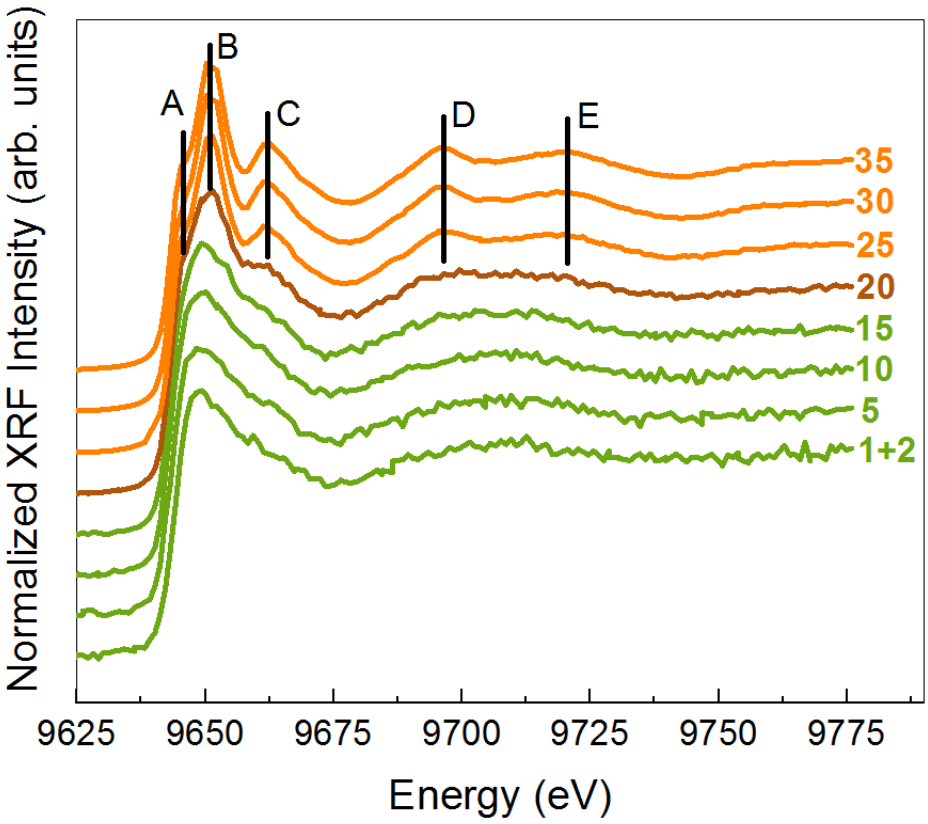

Figure 9: Experimental Zn K-edge XANES spectra for cycles $1-35$ of the ALD growth of ZnO on a $In_{0.53}Ga_{0.47}As$ substrate. All spectra have been normalized to the same jump value at the edge and shifted along the y-axis for clarity. The spectra corresponding to cycle 1 and 2 are nearly identical and were averaged to improve the signal-to-noise ratio. The cycle number is indicated to the right of each spectrum. Embryonic Wurtzite structure (green solid lines), rising of the Wurtzite structure (orange solid lines).

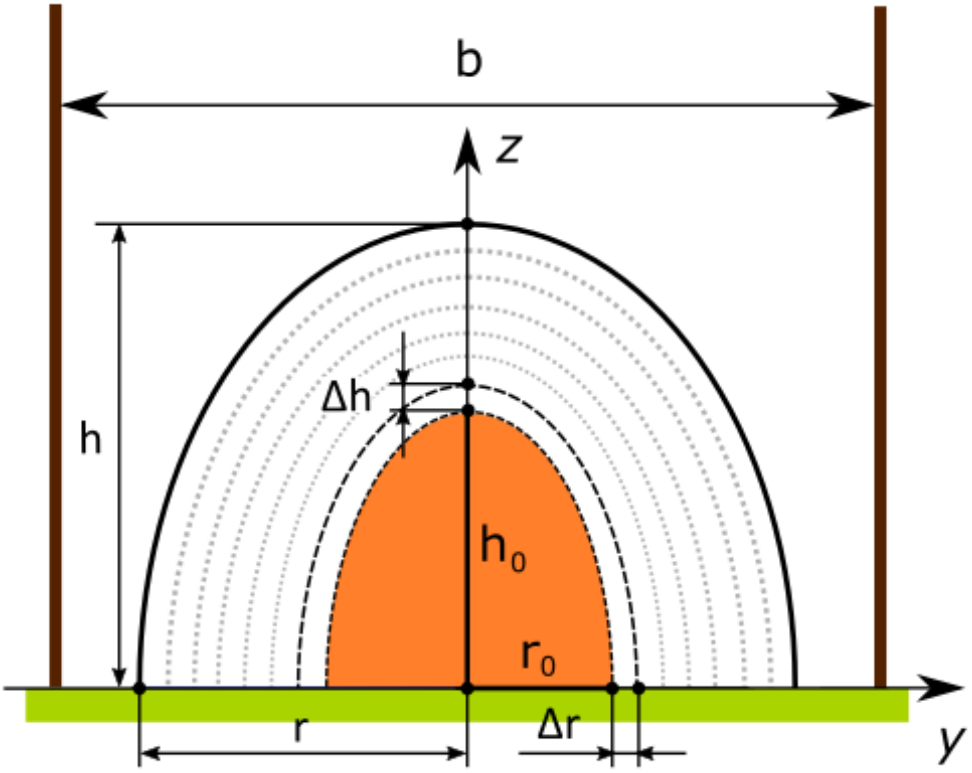

Figure 10: Geometrical parameters of the spheroidal nucleus used in our island growth model: r_0 and h_0 define the size of the nuclei, b is the distance in between 2 nuclei, and Δr and Δh are the incremental increases in the directions parallel and perpendicular to the substrate, respectively, for each ALD cycle (i.e., the GPC).

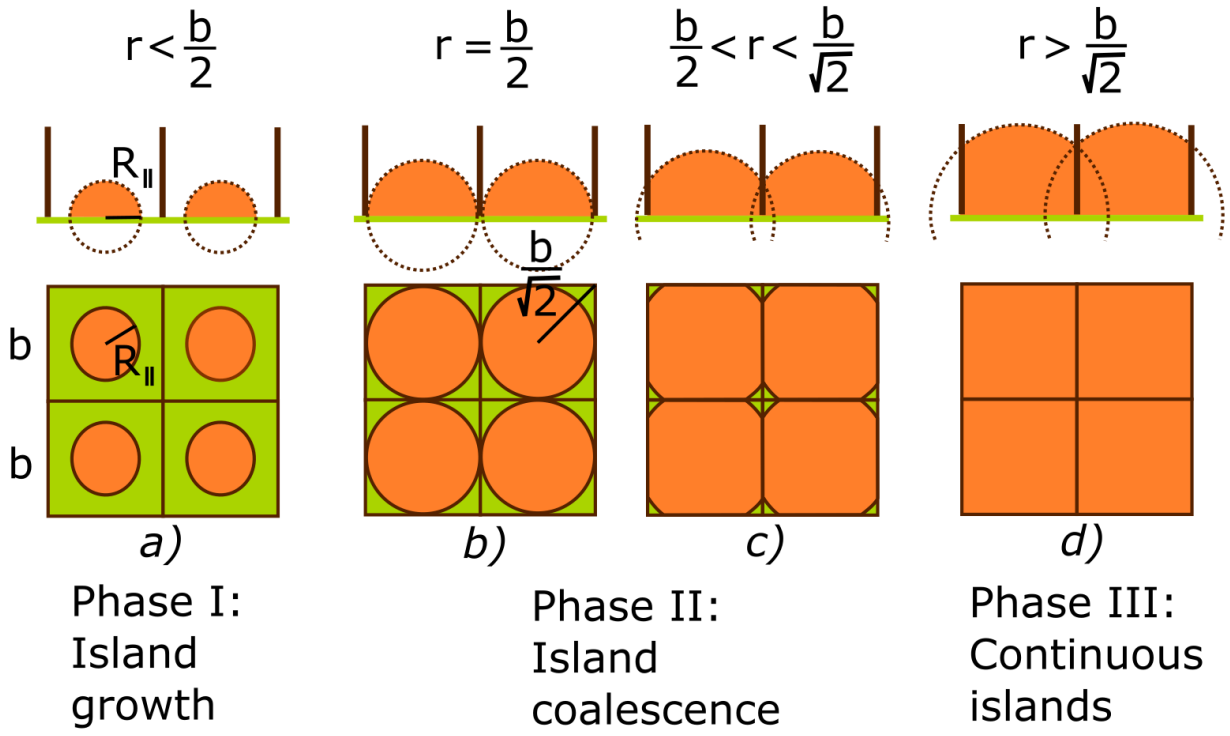

Figure 11: Island growth phases: (a) isolated island growth, (b) and (c) island coalescence, and (d) continuous islands.

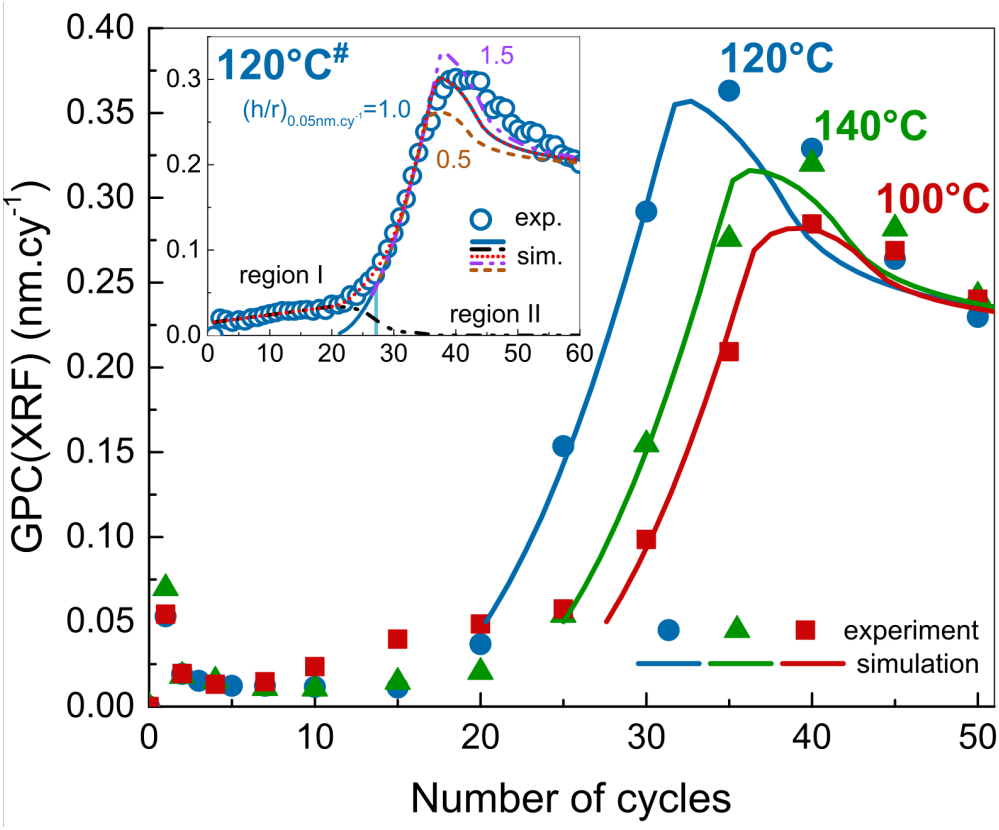

Figure 12: Experimental measurements of growth per cycle (GPCs(XRF)) (filled symbols), and the simulation curves from island growth model (solid lines), as a function of cycle number and for different substrate temperatures (100, 120 and 140°C). The measurements were performed in between growth cycles. The simulation parameters are given in the text. The inset displays the experimental measurement of the GPC performed during growth at $T_{\text{substrate}} = 120°\text{C}$ (open circle). The experimental GPC was shown in Fig. 3 before calibration. Shown are simulated GPC curves for different island aspect ratios, $(\text{h/r})_{0.05}$, at the onset of island growth that corresponds to a GPC close to 0.05 nm.cy^{-1}; $(\text{h/r})_{0.05}$=1 (blue solid line), 1.5 (violet dotted-dashed line) and 0.5 (brown dashed line). The dotted red line is the sum of the blue solid line and the black dotted-dashed line which represents the GPC curve in region I. The GPC simulation curves have been shifted along the horizontal axis to region II by the cycle number of incubation n_{inc}.

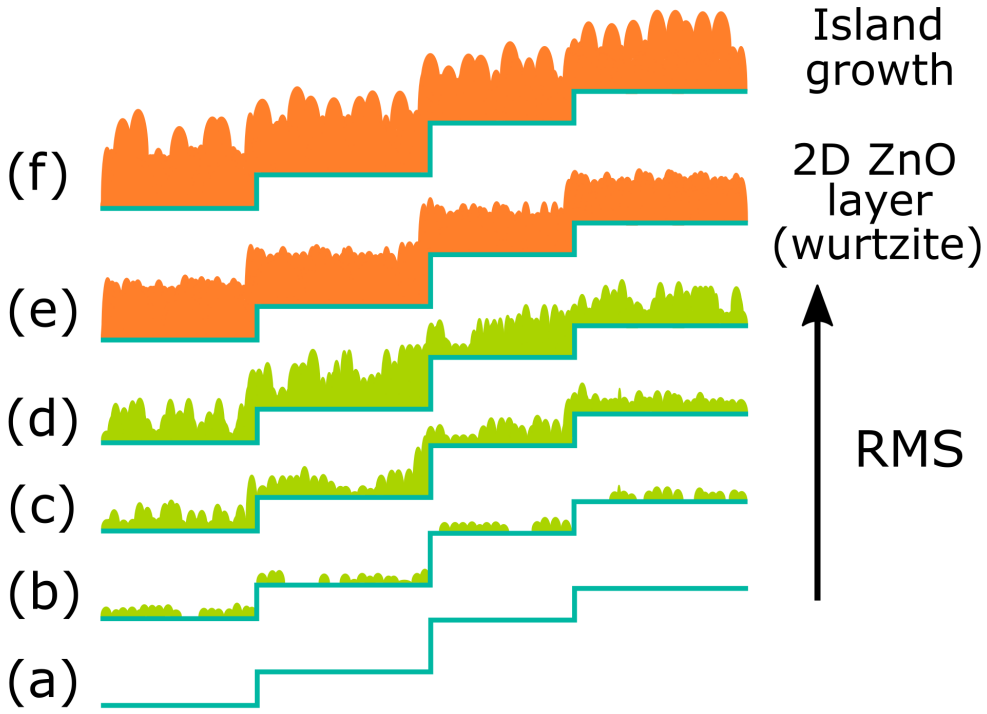

Figure 13: Depiction of the different growth stages: (a) bare $In_{0.53}Ga_{0.47}As$ surface, (b) initial ZnO island nucleation, (c) island density increase, (d) "hole" formation, (d) 2D ZnO layer formation (wurtzite structure), and (f)the island growth phase.

Supplemental Information

The Initial Stages of ZnO Atomic Layer Deposition on Atomically Flat $In_{0.53}Ga_{0.47}As$ Substrates

By E.V. Skopin et *al*.

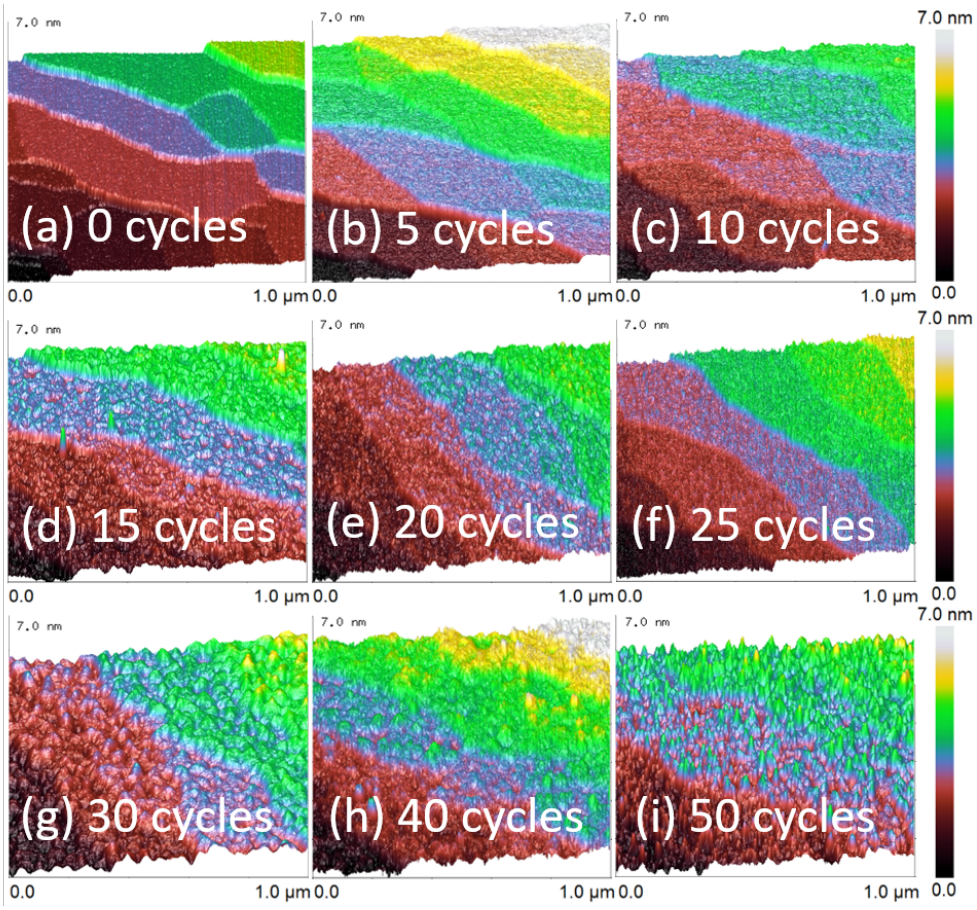

Figure S1. 3D rendering of the same AFM images shown in Fig. 5 of the article, i.e. post-growth AFM images of ZnO films grown on $In_{0.53}Ga_{0.47}As$ for different number of cycles: 0 (a), 5 (b), 10 (c), 15 (d), 20 (e), 25 (f), 30 (g), 40 (h) and 50 (i).

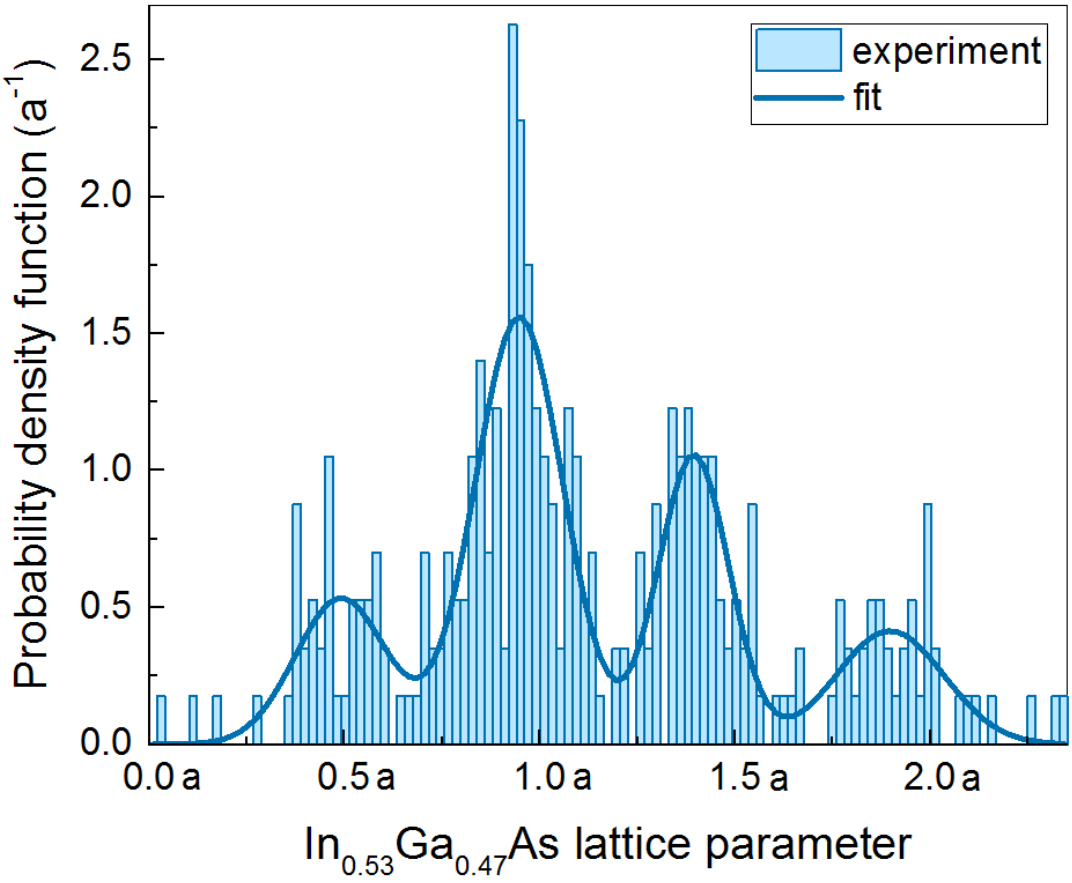

Figure S2. Statistical distribution of the terrace heights present on the $In_{0.53}Ga_{0.47}As$ substrate surface after the 4M HCl etch step. The height value is in *a* units, where *a* is the bulk $In_{0.53}Ga_{0.47}As$ lattice parameter. A series of parallel lines were chosen with a constant distance between the lines for the analysis. The peaks of the statistical distribution have been approximated by a Gaussian function.

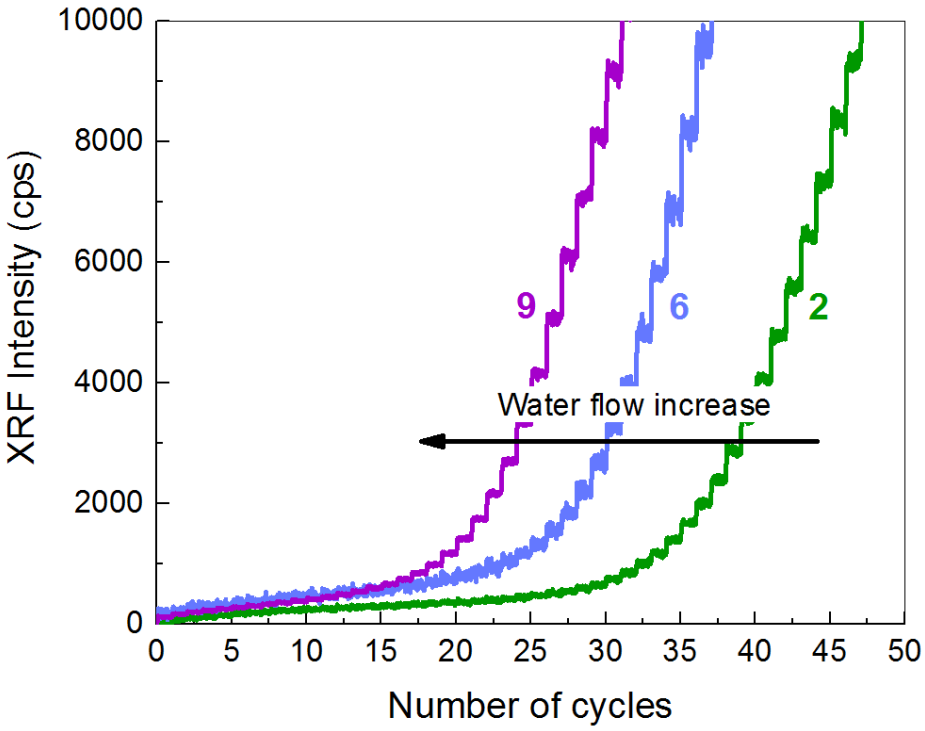

Figure S3: Zn Kα X-ray fluorescence intensity (T substrate = 120°C) vs. cycle number for three different water flow (deionized water). The increasing of water flow is obtained by opening the injector aperture (2, 6, 9 are the numbers of turns of the manual needle valve). Clearly, increasing the water flow shortens the delay in ZnO nucleation.